Quantum solvent states and ro-vibrational spectra of small doped ^{3}He clusters through the Full-Configuration-Interaction Nuclear Orbital approach: the $(^3He)_N$-$Cl_2(X)$ case ($N \leq 4$)

María Pilar de Lara Castells *, Néstor F. Aguirre,

Pablo Villarreal, and Gerardo Delgado Barrio

Instituto de Física Fundamental (C.S.I.C.),

Serrano 123, E-28006, Madrid, Spain

Alexander O. Mitrushchenkov

Université Paris-Est, Laboratoire Modélisation et Simulation Multi Echelle,

MSME UMR 8208 CNRS, 5 bd Descartes, 77454 Marne-la-Vallée, France

(Dated: April 14, 2010)

* Author to whom correspondence should be addressed. E-mail: delara@imaff.cfmac.csic.es

Abstract

A Full-Configuration-Interaction Nuclear Orbital treatment has been recently developed as a benchmark Quantum-Chemistry-like method to study small doped ^{3}He clusters [J. Chem. Phys. **125**, 221101 (2006)]. Our objective in this paper is to extend our previous study on $(^3\mathrm{He})_N$-$\mathrm{Cl}_2(B)$ clusters, using an enhanced implementation that allows employing very large one-particle basis sets [J. Chem. Phys. **131**, 174110 (2009)], and apply the method to the $(^3\mathrm{He})_N$-$\mathrm{Cl}_2(X)$ case, using both a semi-empirical T-shaped and an *ab initio* He-dopant potential with minima at both T-shaped and linear conformations. Calculations of the ground and low-lying excited solvent states stress the key role played by the anisotropy of the He-dopant interaction in determining the global energies and the structuring of the ^{3}He atoms around the dopant. Whereas ^{3}He atoms are localized in a broad belt around the molecular axis in ground-state N-sized complexes with N=1−3, irrespective of using the T-shaped or the *ab initio* He-dopant potential function, the dopant species becomes fully coated by just four ^{3}He atoms when the He-dopant potential also has a minimum at linear configurations. However, excited solvent states with a central ring-type clustering of the host molecule are found to be very close in energy with the ground state by using the *ab initio* potential function. A microscopic analysis of this behavior is provided. Additional simulations of the molecular ro-vibrational Raman spectra, also including excited solvent states, provide further insights into the importance of proper modeling the anisotropy of the He-dopant interaction in these weakly bound systems and of taking into account the low-lying excitations.

Keywords: doped helium clusters, full-configuration-interaction, quantum-chemistry-like, hard-core interaction, ro-vibrational Raman spectroscopy

I. INTRODUCTION

Helium nanodroplets are applied as an ideal cryogenic matrix for high-resolution spectroscopic studies of trapped molecules, extracting remarkable information about the quantum solvent as the manifestation of ^{4}He (^{3}He) superfluid (normal fluid) effects [1] and highlighting the key role of Boson (Fermi-Dirac) statistical effects. In this way, the recovering of a decongested (structured) spectrum for a OCS molecule inside ^{3}He nanodroplets after adding a few tenths of ^{4}He atoms was interpreted as a manifestation of superfluidity at the microscopic scale in doped ^{4}He clusters [2]. Further spectroscopic probes of molecules in rather small $(^4\mathrm{He})_N$-molecule clusters have provided insights into the onset of microscopic superfluidity for just four ^{4}He atoms [3], exploring its possible relationship with the clustering of the ^{4}He atoms at the ends of the dopant molecule at certain cluster size, as analyzed in earlier theoretical studies [4–6]. This research could be further complemented by experimental and theoretical probes of the anisotropy of the He-molecule interactions in small doped ^{3}He clusters.

Accurate theoretical simulations of small and medium-size doped ^{4}He clusters have been provided by stochastic methods such as quantum Monte Carlo (QMC) type treatments [7–9]. In contrast to the ^{4}He isotope, the application of QMC-type methods to doped ^{3}He clusters is problematic because one has to deal with the fermion sign problem arising from the anti-symmetry condition for the wave-function imposed by the Fermi-Dirac statistics so that only upper bounds are obtained within the fixed-node approximation. This is in contrast to quantum-chemistry(QC)-like treatments first proposed by Jungwirth and Krylov [10] that consider the ^{3}He atoms as "pseudo-electrons" and the atoms composing the dopant species as "pseudo-nuclei" (i.e., replacing Coulomb interactions by He-He and He-dopant pair potentials), with all fermionic symmetry effects being automatically included [11]. In the case of $^4\mathrm{He}_2$-diatomic complexes, the main approximations (i.e., the decoupling of the molecular rotation, the adiabatic approach for the stretch diatomic mode, and ignoring potential three-body and higher order terms in the total potential energy function) have been assessed in "exact" variational calculations [12–15]. Within this framework, a Full-Configuration-Interaction Nuclear orbital (FCI-NO) treatment has been recently developed to calculate energies and wave-functions of "solvent" states within small doped ^{3}He clusters with molecular impurities. The main originality of this treatment consists in employing

the Jacobi-Davidson iterative diagonalization algorithm rather than Davidson's (the standard eigen-solver in the electronic structure packages). This provides better convergence in the FCI calculation without sacrificing the repulsive region of the He-He interaction (i.e., properly dealing with the well known hard-core interaction problem), which is the common strategy in other approaches to describe doped He clusters and nanodrops as for example the Hartree/Hartree-Fock treatment [16, 17] or Density Functional Theory (DFT)-based methods [18]. It is worth mentioning that excited solvent states can be calculated through the FCI-NO treatment with a similar precision as the ground-state. Very recently, the computational treatment presented in [19] has been significantly enhanced [20], to include an increasing-orbital-space technique for accelerating the convergence. This allowed the use of much larger basis sets (up to 400 orbitals in clusters comprising up to 4 ^{3}He atoms), and the possibility of calculating one- and two-particle properties as, for example, pair density distributions and magnitudes depending on the He angular momenta, which are necessary to calculate the spectrum of a molecular dopant [16]. The application of this enhanced FCI-NO to small doped ^{3}He clusters with $Cl_2(B)$ and $Br_2(X)$ as the dopant species [20–22] have shown very similar results in both cases owing to the rather similar anisotropic T-shaped character of the used He-dopant potential functions.

One of the goals of this work is to evaluate the influence of using a semi-empirical T-shaped He-dopant potential energy surface (PES) or an *ab initio*-based one, which comprises nearly degenerate minima at T-shaped (T-well) and linear configurations (L-well) on global results, and to analyze the solvent states arising from the transfer of helium density to the ends of a dopant molecule at certain number of ^{3}He atoms. A second objective is to elucidate how the energetic and structural aspects of the helium environment are reflected in the ro-vibrational Raman spectra of the dopant species, including excited solvent states in the simulation as well. For these purposes we have chosen Cl_2 in its ground electronic state as the host molecule by using the two forms of He-Cl_2 potential that were previously compared to experimental data in the He-Cl_2 $B \leftarrow X$ excitation spectra by Huang et al. [23]. Energetic, structural, and spectroscopic aspects of $(^4He)_2$-Cl_2 clusters have been extensively studied both experimentally [24] and theoretically [25–30]. In the case of the dopant in the ground state, a number of theoretical studies on $(^4He)_N$-Cl_2 clusters have been reported [26, 28, 29]. For example, McMahon and Whaley [26] carried out quantum Monte-Carlo calculations on ground and rotationally excited states of $(^4He)_N$-$Cl_2(X)$ (N=1, 6 and 20) by means of a

model T-shaped He-dopant potential, indicating a ground-state ring-like structure perpendicular to the Cl_2 inter-nuclear axis in N=6 sized complexes and showing that the ^{4}He atoms surround the entire dopant for N=20. Later on, full dimensional variational calculations on the $(^4He)_2$-$Cl_2(X,B)$ tetramers at zero total angular momentum were performed by Hernández et al. [28], revealing the importance of considering the ^{4}He permutation symmetry in order to properly simulate the $B \leftarrow X$ excitation spectra. More recent path-integral Monte-Carlo simulations were carried out by Takayanagi et al. [29] on ground-state energies and one-particle density distributions on medium-sized clusters ($N < 100$), suggesting that ^{4}He atoms are mainly localized around the saddle point regions for N=10 (within the first solvation shell), and the formation of a second and third more isotropic shells for N=40 and 100. No previous studies exist on $(^3He)_N$-$Cl_2(X)$ clusters with fermionic exchange effects, which are taking into account in this work.

II. OUTLINE OF THE METHOD

As in electronic structure problems, we first solve the Schrödinger equation for the N ^{3}He atoms clustering a diatomic molecule, AB, at fixed values of its bond-length, r;

$$\left[H^{(N)} - E^{(N)}_{\Lambda,S}(r)\right] \Phi^{(N)}_{\Lambda,S}(\{\mathbf{R}_k\}; r) = 0 \tag{1}$$

where S is the total spin angular momentum of the He atoms. $H^{(N)}$, the analog to the electronic Hamiltonian, can be written as:

$$H^{(N)} = \sum_{k=1}^{N} \left(K_k(\mathbf{R_k}) + V_k^{\mathrm{AB-He}}(\mathbf{R_k}; r)\right) + \sum_{k\leq l} V_{kl}^{\mathrm{He-He}}(|\mathbf{R}_k - \mathbf{R}_l|) - \frac{\hbar^2}{m_{AB}} \sum_{k<l} \nabla_k \cdot \nabla_l \tag{2}$$

where $\mathbf{R_k}$ are the vectors from the diatomic center of mass to the different He atoms. $H^{(N)}$ therefore comprises one-particle kinetic, K_k, and potential energy terms, $V_k^{\mathrm{AB-He}}$, as well as two-particle potential, $V_{kl}^{\mathrm{He-He}}$, and kinetic energy coupling, $\nabla_k \cdot \nabla_l$, terms. The r-dependent eigenvalues and eigenfunctions are labeled according to the projection of the total orbital angular momenta $\mathbf{L}$=$\sum_N \mathbf{l}_k$ on the molecular axis Λ and S. For a total angular momentum $\mathbf{J}$=$\mathbf{j}$+$\mathbf{L}$+$\mathbf{S}$ ($\mathbf{j}$ being the diatomic angular momentum) with projection onto the BF Z-axis $\Omega = \Lambda + \Sigma$ (Σ being the projection of S on Z), omitting Coriolis couplings, the effective Hamiltonian of the dopant molecule can be written as,

$$H_N^{eff} = -\frac{\hbar^2}{2m}\frac{\partial^2}{\partial r^2} + U(r) + E^{(N)}_{\Gamma,S}(r) + \frac{\hbar^2}{2mr^2} G. \tag{3}$$

Neglecting non-adiabatic (i.e., $\mathbf{L}_+ \cdot \mathbf{S}_- + \mathbf{L}_- \cdot \mathbf{S}_+$) corrections and averaging $\mathbf{L}$ over the total helium wave-function at r=r$_e$, G is approximated by,

$$G \approx J(J+1) + \langle \mathbf{L}^2 \rangle - 2(\Lambda^2 + \Sigma^2 + \Lambda\Sigma). \tag{4}$$

In order to solve Eq. 1 within a one-particle basis representation we applied the FCI-NO method presented in [19] and extended in our recent paper [20], to which interested readers may refer to.

The modified Schrödinger equation $\left[H_N^{eff} - \epsilon_{JS\Lambda\Sigma v}\right] \chi_{JS\Lambda\Sigma v}(r) = 0$ is then solved to calculate the dopant eigenvalues and ro-vibrational spectra as presented elsewhere (for example see [16]). In contrast to previous studies, however, the r-dependence of the E$^{(N)}_{\Gamma,S}$ eigenvalues in Eq. 3 was neglected. Since we focused on the vibrational excitation v =1 $\leftarrow$ 0 of Cl_2, the relevant r range being very narrow and the energy r-dependence of the energy for the quantum solvent states being very weak, this is a reasonable approximation. For a fixed energy of the incident photon we considered a Boltzmann distribution over solvent states at a given temperature T and averaged over initial rotational states. In order to obtain continuum profiles, we have assumed a generic relaxation process by dressing the stick spectral lines for the ^{3}He-$Cl_2(X)$ triatomic with Lorentztians functions with associated half-width $\Gamma_1/2 = 1.5 \times 10^{-3}$ cm^{-1}. Hereafter, the line broadening of a N-sized complex is assumed to be N times that of the triatomic, $\Gamma_N/2 \sim N \times \Gamma_1/2$, and the stick spectral lines are dressed with Lorentztians using these calculated widths.

III. POTENTIAL ENERGY SURFACES AND NUMERICAL DETAILS

The $Cl_2(X)$ interaction was described by a Morse function [31], $U(r) = D\left\{1 - e^{-\alpha(r-r_{eq})}]\right\}^2 - D$, whereas for the He-$Cl_2(X)$ PES a semi-empirical He-dopant model PES or an *ab initio* one was employed. Contour plots of the two He-dopant PESs as a function of the Jacobi coordinates (R, θ) are displayed in Figure 1. The model PES is built as a pair-wise addition of the He-Cl(X) V$_\Sigma$ potentials as proposed by Aquilanti et al. [32]. The form of this He-Cl(X) potential is V=V$_0$ + 0.4 V$_2$, where V$_0$ is a potential energy term of the Morse-Spline-van der Waals form and V$_2$ is a (exp,6) Buckingham-type model potential. The resulting He-$Cl_2(X)$ PES is rather anisotropic (see left panel of Fig. 1) with a single minimum of ~ -38.8 cm^{-1} at a T-shaped geometry (R$_e$=3.4 Å) which gradually decreases

up to ~ -21.8 cm^{-1} (R$_e$=4.5 Å) at linear configurations. The Cl-Cl bond length was fixed to its equilibrium value in the ground electronic state [25, 31] (1.99 Å). As a second approach, we used the He-Cl$_2$(X) PES fitted to *ab initio* calculations by Huang et al. [23], which uses the Morse-Spline-van der Waals parameterization of Beneventi et al. [33]. This PES comprises two minima (see rigth panel of Fig. 1): a global minimum of ~ -40.5 cm^{-1} at a linear configuration (R$_e$=4.2 Å), and a secondary minimum at a T-shaped configuration of ~ -36.6 cm^{-1} (R$_e$=3.4 Å), with a saddle point of about -17 cm^{-1} between the minima. It should be mentioned that there are improved *ab initio* He-Cl$_2$(X) PESs based on high-level *ab initio* calculations [29, 34]. These potentials are similar around the T-well regions and differ at regions close to the global minimum at the linear configuration, which is found to be deeper in most accurate *ab initio* calculations. However, zero-point energy effects reverse the relative stability of the corresponding quantum states (see below). The *ab initio*-based PES of [23] is considered good enough as an example of a He-diatomic interaction with minima at both T-shaped and linear configurations although a careful comparison with possible spectroscopic measurements on (^{3}He)$_N$-Cl$_2$(X) complexes would probably require the use of a more accurate potential.

As in our previous applications of the FCI-NO method (see [20]), a basis set comprising numerical radial functions and spherical harmonics $Y_{\ell m}(\theta, \phi)$ was used. The radial functions, F_n ($n = 1 \ldots n_{max}$), were constructed by orthogonalization of the lowest-energy solutions of the radial Schrödinger equation for the ^{3}He-AB triatomic at fixed angular orientations of the He atoms with respect to the diatomic, θ_n, as described in detail in [17] and [27]. Our previous studies showed that a very large basis representation comprising at least $n_{max} = 4$ radial functions and saturated angular functions ($m_{max} = \ell_{max}$) with $l_{max} = 8$ were necessary to get converged results. Therefore, the same basis representation was employed here (i.e., a total of 324 orbitals). With this very large basis set, we are able to perform the Full-CI calculations considering up to four ^{3}He atoms (with a FCI space of about 2×10^8 configuration state functions). As mentioned in Ref. 20, work is in progress to implement an extended version of the FCI-NO method that, using an optimized basis set, allows the calculation of larger clusters. We used m$_{\rm Cl}$=35.4537 amu, and m$_{^3{\rm He}}$=3.01604 amu. In the case of employing a semi-empirical He-dopant potential, the chosen set of θ_n values is $\theta_n = \pi/2 - (n-1)\pi/24$ to properly describe the neighborhood of the T-shaped equilibrium angular region. Whereas n_{max} equidistant values of θ_n in the range $[0, \pi/2]$ were used to

describe both the T-well and the L-well equilibrium angular regions when modeling the He-Cl_2 interaction with an *ab initio* PES. The convergence thresholds for the total energies, $E^{(i)} - E^{(i-1)}$ (i denoting the ith outer Jacobi-Davidson iteration [19]), was set to 10^{-9} cm^{-1}. Within this threshold, the norms of the residual vectors (defined as $(E - \hat{H})\mathbf{C}$) were less than 3×10^{-3} cm^{-1} in all cases.

In order to simulate the ro-vibrational Raman spectra a temperature of 0.5 K, which is over the transition temperature to super-fluidity of ^{3}He ($T_\lambda = 3 \times 10^{-3}$ K from [35]), was assumed to perform the simulations. Values for the total angular momentum $J \leq 10$ were included in the calculations to achieve convergence at that temperature. The necessary polarizabilities of the dopant, assumed to be unchanged by complexation, were taken from [36].

IV. QUANTUM SOLVENT STATES

The FCI-NO approach was applied to the calculation of the energies and helium wave-functions of $(^3\text{He})_N$-$Cl_2(X)$ clusters, $N \leq 4$, in their ground and low-lying excited states, with all possible spin multiplicities, using both T-shaped model and *ab initio* He-dopant potentials. The different states have been classified according to the number of fermions (N), the total spin (S) and the irreducible representations within the D_{2h} symmetry group. A summary of the FCI results by using a T-shaped model potential are presented in Table I, which lists the FCI energies associated to the lowest- and first-excited states within each (N, S) manifold, the occupation numbers τ of the relevant effective "nuclear" natural orbitals (NOs) (the eigen-vectors of the first-order reduced density matrix) for the lowest-energy states and the average values $\langle \mathbf{L}^2 \rangle$ for lowest- and first-excited states, which are necessary to simulate the dopant Raman spectra.

A selection of FCI results for $(^3\text{He})_N$-$Cl_2(X)$ clusters, with an *ab initio* He-$Cl_2(X)$ PES, is displayed in Tables II−IV and Figs. 2−6. The FCI energies for the lowest-energy state within each irreducible representation of the D_{2h} symmetry group and (N, S) manifold are listed in Table II. The states that are symmetric (antisymmetric) under reflexion on a mirror plane perpendicular to the dopant molecular axis have been marked with $\kappa = \pm 1$. In Table II we also show the averaged values of the squared orbital angular momentum, $\langle \mathbf{L}^2 \rangle$, associated to FCI states for N=4. The occupation numbers τ of relevant NOs corresponding to the

lowest-energy states of the different (N, S) manifolds are given in Table III. Table IV lists the kinetic $\langle K \rangle$ and potential contributions to the total energy of the lowest and selected excited states for all cluster sizes. The potential term is separated in dopant-helium $\langle V^{\mathrm{He-Cl_2}} \rangle$ and helium-helium $\langle V^{\mathrm{He-He}} \rangle$ contributions. The upper panel of Figure 2 displays the angular and radial (inset panel) one-particle helium density distributions around the guest molecule in the lowest-energy states, whereas the lower panel shows iso-probability surfaces of the ground-state density for N=3 and 4. Figure 3 shows iso-probability surfaces associated to the most important NOs for the ground state of the $(^3\mathrm{He})_4$-$\mathrm{Cl_2}(X)$ cluster. In Figure 4 we display the angular and radial (inset panel) one-particle helium density distributions around the guest molecule for all the states and cluster sizes that we have considered. Finally, we plotted all the probability density distributions $\mathrm{D}(cos\gamma_{12})$ as a function of the angle between the position vectors of two helium atoms γ_{12} and the pair density distributions as a function of the inter-particle distance $\mathrm{D}(R_{12})$ in Figs. 5 and 6, respectively.

A. Quantum solvent states using a T-shaped model He-dopant potential

As mentioned above, the lowest FCI energies and the excitation energies with respect to the first excited state within each (N,S) manifold are displayed in Table I. Overall, very similar results to those found for clusters with $\mathrm{Cl_2}(B)$ as the dopant species have been found. Hence, a comparison with Table I of [20] clearly shows that the symmetries of the ground and the first excited states are the same, regardless the electronic state of the dopant. Additionally, the excitation energies of the first excited state, $\Delta\mathcal{E}$, for each (N,S) manifold are very close, with those corresponding to the X state being slightly larger. In particular, with the exception of the $^5\Delta_g$ and $^5\Pi_u$ states for N=4, all the $\Delta\mathcal{E}$ values are within 0.03 cm^{-1}. This result reflects the similarity of the energy level structure of the corresponding lowest N=1 eigenstates that in turn, is due to a rather similar anisotropic T-shaped character of the used He-dopant potential energy surfaces. In this way, the energy difference between the $1\sigma_g$ and the $1\pi_u$, $1\delta_g$, and $1\phi_u$ orbitals are of 0.46 (0.44), 1.60 (1.57) and 3.65 (3.56) cm^{-1} for the $X(B)$ state. As mentioned in previous studies [20, 37], the first one-particle energy levels are roughly rotational energy levels of a rigid rotor (i.e., involving rotations on the plane perpendicular to the inter-nuclear $\mathrm{Cl_2}$ axis) on a reduced one dimensional (1D) model implying only the azimuthal angle ϕ_i (hereafter referred to as 1D-rotor-like states).

Within this model, the energy difference between the lowest $1\sigma_g$ (ℓ_z=0) and the excited ($\ell_z > 0$) one-particle states can be approximated (within a relative error of about 10%) by $B_{\rm eff} \times \ell_z^2$, where $B_{\rm eff}$ is an effective rotational constant that is proportional to the expectation value of $\langle \frac{1}{2\mu R^2} \rangle$ on the corresponding zero-energy level $1\sigma_g$ state. We wish to stress here that radial one-particle density distributions on the $1\sigma_g$ states are peaked at very similar values [3.85(X) *vs.* 3.89 cm^{-1}(B)], the $\langle R \rangle$ expectation values being also very close (4.04 *vs.* 4.11 cm^{-1}). As a result, the effective $B_{\rm eff}$ constant is only slightly larger (by 0.01 cm^{-1}) for the X state. If we now compare the τ values of Table II with those presented in [20], we can see that they differ by 0.04 at the most. This is not significant considering that the maximum differences between the values attained for $\ell_{max} = 8$ and 9 are of the same order of magnitude. The repulsive effective on-site interaction arising from the sharply repulsive He-He wall, which is obviously the same for the dopant in the ground and excited electronic states, suppresses the double occupation of the orbitals in such a way that τ values of the most relevant (N) NOs approach unity as the cluster grows in size. This is in analogy to the fermionic Hubbard Hamiltonian model [38] for strongly interacting electrons in a periodic lattice. On the other hand, a further delocalization of τ values over orbitals with higher ℓ_z values is mainly due to the weak attractive region of the He-He potential making the average He-He interaction negative. Very similar results were also obtained for $Br_2(X)$ as the dopant species and a T-shaped model potential function in [22]. As mentioned in [20], the lowest-energy spin states for any N, showing a very similar degeneracy degree when using T-shaped model potentials for Br_2 and Cl_2 as dopant species, have nearly indistinguishable pair density angular and radial distributions (see for example Figs. 2 and 3 in [22]). In this way, average values $\langle V^{\rm He-He} \rangle$ between all the lowest-energy spin states are very close. Thus, for example, for N=4 they differ by less than 1.5%. Furthermore, the He-dopant energy contribution can be approximated to better than 2% to that of N triatomics in the $1\sigma_g$ state, for all the calculated states. Therefore the lowest-energy spin states differ mostly in the average $\langle K \rangle$ contribution. Whatever the cluster size and spin multiplicity be, the ground-energy states are always of Σ symmetry (i.e., $^1\Sigma_g^+$, $^4\Sigma_g^-$, and $^3\Sigma_g^-$ for N=2, 3 and 4, respectively). A further analysis of the wave-function structure in terms of a reduced dimensional model that decouples the azimuthal degrees of freedom from the rest (similar to the one presented in [27, 28] for two ^{4}He atoms) shows that the higher energy Π and Δ states resemble overall rotations around the Z axis with an excitation energy approximately

given by $\frac{B_{eff}\Lambda^2}{N}$. As a result, the two lowest energy states for N=2 (3) differ by 0.23 (0.15) cm^{-1} which is a half (a third) of the energy difference between the $1\sigma_g$ and the 1π state (i.e., 0.46 cm^{-1}). The same holds true for the $^5\Delta_g$ state (N=4), in which the $^{3,1}\Sigma_g^{+,-}$ states remain practically degenerated. It is worth noticing that these quantum solvent states are forbidden for clusters composed of spin-less ^{4}He atoms due to the symmetry condition for the wave-function imposed by Bose statistics. For example, the spatial components of the wave-functions for the $^3\Pi$ (N=2) and the $^5\Delta_g$ (N=4) states, which obviously can be decoupled from the spin part, are anti-symmetric. The excitation modes of He atoms in the $^3\Pi_u$ and $^1\Delta_g$ states for N=4 can also be assigned to global excitations around Z with a promotion energy of about a quarter of the energy difference between the $1\sigma_g$ and the 1π and $1\delta_g$ orbitals. In the same way, the energy difference between the $^2\Delta_g$ and $^4\Phi_g$ states and the ground state could be approximated as $\frac{B_{eff}\Lambda^2}{3}$, with predicted values of 0.6 and 1.2 cm^{-1}, falling in line with the actual values shown in Table I. Globally, all excited states within the low-energy edge of the excitation spectrum for N=3 could be correlated to those of an "effective" fermionic particle (i.e., the total spin of the complex is half-integer) of mass $3\times m_{^3He}$. The fact that the rotational excitations are around the molecular axis is clearly demonstrated by the expectation values $\langle \mathbf{L}_x^2 + \mathbf{L}_y^2 \rangle$, which are quite close between states within the same cluster size, as can be inferred from Table I. The wave-function structure of the second and third excited states for N=2 and the $^5\Pi_u$ state for N=4 is more complex because, along with global excitation around the Z axis, He-He bending excitations are also involved.

Overall, as in previous studies with $Cl_2(B)$ and $Br_2(X)$ as dopant species, global results show that the favored clustering of ^{3}He around the dopant species in the ground and in low-lying excited states is such that the He-dopant potential interaction is maximized, forming a delocalized equatorial ring around the dopant axis. In this way, the $\langle V^{He-Cl_2} \rangle$ values for any N are approximately N times the value attained for the zero-energy level of N=1. In line with previous results by McMahon and Whaley [26], when using a quite similar T-shaped He-Cl_2 potential, we found that ring-like structures are practically unchanged by small rotational excitations (around the Z axis in our case). Departing from the classical picture of He atoms occupying equivalent positions on the annular ring, ^{3}He atoms tend to form pairs on the broad belt around the dopant in order to also benefit from the very weak He-He attractive part of the potential, with the average He-He interaction per pair

being negative and scaling linearly with N. These short-range correlation effects raise the $\langle K \rangle$ average (i.e., due to promotion to orbitals with high m values), which is somewhat counterbalanced by the negative $\langle V^{\mathrm{He-He}} \rangle$ contribution, resulting in a quasi-linear scaling of ground state total energies with the number of particles. Consistently, the averaged values of the squared orbital angular momentum, $\langle \mathbf{L}^2 \rangle$, corresponding to the lowest-energy states also increase almost linearly with the cluster size N.

B. Quantum solvent states using an *ab initio*-based He-dopant potential

1. *Independent-particle N=1 states*

As mentioned above, the *ab initio*-based PES [23] mainly differs from the semi-empirical PES in posing both T- and L-wells, with the strengths of the He-dopant interaction at the T-shaped minimum differing by only 1.7 cm^{-1}. Although the L-well is deeper by ~ 4 cm^{-1}, Table II clearly shows that zero-point energy effects reverses the order of stabilities of the T- and L-wells and the ground T-shaped $N = 1$ eigen-state (the $1\sigma_g$ orbital whose density is represented in Figs. 2 and 4) becomes about 1.7 cm^{-1} more stabilized than the lowest N=1 state with an associated density mainly located at a linear configuration (the $2\sigma_g$ orbital in Fig. 4).

By focusing on the Z-symmetric ($\kappa = +1$) excited orbitals of Table II and the two first columns of Table III, we see that the $\ell_z > 1$ independent-particle orbitals can be assigned to 1D-rotor-like states, as when using a model T-shaped potential (see above). Consequently, they differ mostly in the azimutal part, with the angular D(θ) and radial D(R) density distributions being very similar (see Fig. 5). As in the case of the T-shaped potential, the estimated $\mathrm{B_{eff}}$ is close to 0.4 cm^{-1}.

On the other hand, the $2\sigma_g$ orbital and the lowest-energy ($\kappa = -1$) $1\sigma_u$ orbital are localized on the linear minimum regions of the *ab initio* PES. Therefore, the D(θ) distributions display two peaks close to θ=180° and 0°, the D(R) density being shifted by about 0.6 Å with respect to the T-shaped orbitals. Table II shows that these two orbitals are almost degenerate, with the energy difference being about 0.04 cm^{-1}. This is expected due to the negligible overlapping between very distant orbitals located at the chlorine ends. Finally, the $\kappa = -1$ $1\pi_g$ and $1\delta_u$ orbitals are mainly localized on the saddle point regions of the

He-dopant potential albeit a bit polarized towards the L- and T-well regions, respectively (see Fig. 4). Their energies are rather high and therefore the corresponding occupation numbers are negligible in any of the N $\leq$ 4 states considered in this work. Although it can be expected that these orbitals will be populated for larger cluster sizes (i.e., giving rise to the formation of two lateral rings around the dopant) we found no sign of the existence of ground state densities peaked only at the saddle point regions for N > 4, as found in [29] for a $(^4He)_N$-Cl_{10} cluster through finite-temperature path-integral Monte-Carlo calculations, using an *ab initio* potential which attains a deeper well at linear configurations.

2. Lowest-energy solvent states

When focusing on the results associated to the ground solvent states in Table II, we find that the total energies scale almost linearly with the number of He atoms and that these states always correspond to $\Lambda = 0$ (i.e., they are Σ states). By comparing Tables I and II, we can see that, regardless of the used PES, the ground solvent states have the same symmetry. Up to N=4, the ground states are very similar to those obtained by using model T-shaped potentials. As clearly shown in the top part of Fig. 2, the local angular densities near the impurity are highly structured and peak around $\theta = 90°$. The ^{3}He atoms in the lowest-energy states only populate this attractive well up to N=3. In this way, the radial distributions peak at almost the same value as for the independent particle $1\sigma_g$ state (R $\sim$ 3.9 Å). See the inset of Fig. 2. By comparing the results displayed in Table I and III, we also observe that τ values are very close when using T-shaped or *ab initio* He-Cl_2 PESs with N up to 3. As in the T-shaped model PES case, the $\langle V^{\mathrm{He-Cl_2}}\rangle$ contribution to the total energy (see Table IV) can be approximated as N times the $\langle V^{\mathrm{He-Cl_2}}\rangle$ value for the zero-energy N=1 level (within 2%). Up to N=3, both angular and radial pair density distributions associated to the ground solvent states (see Figs. 5 and 6) are also very similar to these obtained not only for $Cl_2(X)$ but also for $Cl_2(B)$ and $Br_2(X)$ as dopants by using T-shaped potential functions to model the He-dopant interaction [20, 22]. Thus, radial pair densities, $D(R_{12})$, peak at $\sim 2\times R_{eq}^T$ (R_{eq}^T being the equilibrium distance on the T-well) and develop a shoulder at $\sim 2\times R_{eq}^T\times\ sin(\frac{\gamma_{12}}{2})$ ($\gamma_{12} = 70°$), correlating with the second feature located at $cos(\gamma_{12}) \sim 0.35$ in the angular pair densities (compare Fig. 5 with Fig. 6 of [20]). As a result, $\langle V^{\mathrm{He-He}}\rangle$ contributions to the total energies differ by less than 0.02 cm^{-1} to those

obtained, for example, for the $Br_2(X)$ case (see Table III of [22]).

a. The special case of the $^3\Sigma_g^-$ state for N=4 By comparing Tables I and II, we can see that the ground solvent state for N=4 is also a $^3\Sigma_g^-$ state. However, the characteristics of this state differ significantly from those obtained with a T-shaped potential. As clearly shown in Fig. 2, a portion of the ground-state density flows from the T-configuration into the linear ones, so that two side peaks appear at θ values close to 0° and 180° and the radial density distribution exhibits a maximum which is slightly shifted outwards. The transition from a ring-shape coating for N=3 to a fully dopant solvation for N=4 is clearly apparent in the iso-probability surfaces that are shown at the bottom of Fig. 2. We can also notice that the ^{3}He atoms are rather delocalized over the ring. Hereafter, the states with a ring-shaped density will be referred to as ring-like states while the states posing density at the two Cl_2 ends will be denoted as ring-stacker-like states. The analysis of natural orbitals and associated τ values for this $^3\Sigma_g^-$ state is a bit more involved than in the model PES case. A plot of iso-probability surfaces corresponding to the relevant NOs is given in Fig. 3. In contrast to the T-shaped potential case in which the relevant NOs differ only slightly from the N=1 independent-particle orbitals [20], the mixing of the original $1\sigma_g$ and $2\sigma_g$ orbitals is clearly apparent in Fig. 3. This hybridization results in two stabilized natural orbitals with a belt-shaped ring and two lobes at the chlorine ends. By comparing τ values in Tables I and II for this state, we can see that the population of $1\delta_g$ and $1\phi_u$ equatorial NOs significantly decrease when the $2\sigma_g$ is being populated. In contrast, the $1\pi_u$ orbital occupation number increases. As a consequence of the population of the regions near the two poles of the molecule, the angular pair density distribution (see Fig. 5) develops a second maximum at θ_{12}=90° (i.e., the most probable angle between a He atom on the ring and another atom on one of the two lobes at the Cl_2 ends).

b. Energy partition analysis from N=1 up to N=4 In order to better understand why the $^3\Sigma_g^-$ state is more stable than a ring-like one for N=4, we compare the $\langle K\rangle$, $\langle V^{\mathrm{He-Cl_2}}\rangle$ and $\langle V^{\mathrm{He-He}}\rangle$ contributions to the total energy between the lowest-energy ring-like states and those posing ^{3}He density at the two ends of Cl_2 in Table IV. As compared with the $1\sigma_g$ ring-like orbital, the $2\sigma_g$ orbital attains a less attractive average He-dopant interaction. As a consequence, regardless the numbers of particles, ring-like states have more negative $\langle V^{\mathrm{He-Cl_2}}\rangle$ values. The opposite holds true for the $\langle K\rangle$ expectation values up to N=3. The He-He contribution per pair scale almost linearly for ring-like states with a very similar

rate to that found by using T-shaped He-dopant potentials for Cl_2 and Br_2. On the other hand, the average He-He interaction between n ^{3}He atoms localized on the ring and one ^{3}He atom on the two ends of the molecule, which is also negative owing to the attractive long-range region of the He-He potential, scales almost linearly with n. Indeed, as the cluster grows in size the He-He interaction becomes more attractive on ring-like states. However, as analyzed in previous studies [20, 22], the linear behavior of the He-He contribution per pair in ring-like states is at the expense of populating orbitals with very high m values, eventually raising the average kinetic contribution. Therefore, for N=4, the increased average kinetic energy for the ring-like $^1\Sigma_g^+$ state is not compensated by the higher He-He and He-dopant attraction and the $^3\Sigma_g^-$ state becomes 0.26 cm^{-1} lower in energy. Overall, the appearance of helium density at the ends of the molecule could be interpreted as the result of a competition between short- and long-range ^{3}He-^{3}He correlation effects.

c. Lowest-energy spin multiplets Up to N=3, all the lowest-energy spin states have the same characteristics than those obtained with a T-shaped He-Cl_2 potential. Thus, τ values are practically the same (compare Tables I and III). The same holds true for the pair densities that can be compared to those presented in [20] and [22], also using T-shaped He-molecule potential functions. Once again, this similarity corroborates the major role of dynamical short-range correlations effects between the ^{3}He atoms encircling a molecule. For N=4, not only the lowest-energy triplet but also the singlet and quintet states are very different to those obtained when using a T-shaped potential. For example, the lowest energy quintet state is a Σ_u^- state, whereas the Δ_g state, which is the lowest quintet state when using a semi-empirical PES, is about 0.6 cm^{-1} higher in energy. The lowest-energy states with maximum spin un-pairing have a single-reference configuration. The $^5\Delta_g$ state is approximately described by a $(1\sigma_g)(1\pi_u^2)(1\delta_g)$ reference configuration, whereas the Σ_u^- one is dominated by a $(1\sigma_g)(1\pi_u^2)(1\sigma_u)$ configuration (see Table III). In an effective one-particle picture, the energy ordering of these two states reflects the competition between $(1\delta_g)$ and $(1\sigma_u)$ orbitals to accommodate one ^{3}He atom. The $1\delta_g$ orbital is slightly lower in energy (-8.9 *vs.* -8.6 cm^{-1}) whereas the hard-core repulsion between a ^{3}He atom located near the poles of the dopant and another one on the equatorial ring is spatially suppressed, as compared to that between He atoms on the broad belt encircling the dopant. The second factor is expected to be increasingly more important as the cluster size increases (i.e., the effective on-site interaction on the $1\delta_g$ orbital is increasingly more repulsive as

the annular ring becomes more crowded). Thus, the $^3\Delta_g$ state for N=2, dominated by a $(1\sigma_g)(1\delta_g)$ configuration, becomes 0.2 cm^{-1} lower in energy than the $^3\Sigma_u^+$ state, which is well described by a $(1\sigma_g)(1\sigma_u)$ reference configuration. On the other hand, the $^4\Pi_u$ state for N=3, dominated by a $(1\sigma_g)(1\pi_u)(1\sigma_u)$ configuration, becomes 0.07 cm^{-1} lower in energy than the $^4\Phi_u$ state, which can be approximately described by a $(1\sigma_g)(1\pi_u)(1\delta_g)$ reference configuration. Actually, a further partition of the total energy shows that the average He-He interaction, as well as the average He-dopant interaction, is more attractive in the ring-like $^3\Delta_g$ and $^4\Phi_u$ states than in the ring-stacker-like $^3\Sigma_u^+$ and $^4\Phi_u$ states so that the transition to a "full-coated" regime is not due to a larger He-He repulsion but to the fact that the comparatively larger kinetic energy contribution for ring-like states is no longer counterbalanced by the more attractive He-dopant and He-He interactions at certain cluster size.

It is also interesting to compare τ values between the (N,S) pairs (3,1/2)/(4,0) and (3,3/2)/(4,2) in Table III. In fact, we can see that for both pairs the τ values for N=3 NOs, located around the equator of the molecular axis, are practically conserved. For N=4, the additional ^{3}He atom in the lowest energy (4,0) and (4,2) states populates $2\sigma_g$ and $1\sigma_u$ orbitals, with the corresponding occupancies approaching one. Actually, for most states, the $2\sigma_g$ and $1\sigma_u$ NOs are very close to the $2\sigma_g$ and $1\sigma_u$ independent-particle orbitals (with τ values being ~ 0.99). For N=4, we only found two cases with significant mixing between $1\sigma_u$ and $2\sigma_g$ orbitals: the $^3\Sigma_g^-$ ground-state and the $^1\Delta_g$ state. Once again, the adiabatic conservation can be qualitatively understood by taking into account that the short-range correlation between a ^{3}He atom located at the poles of the dopant and those filling the equatorial ring is spatially suppressed.

Figs. 4−6 clearly show that the density distributions attained by the lowest-energy spin multiplets for N=4 are quite similar. Major differences are found for the $^4\Sigma_g^-$ state, with the D(R) and D($cos\gamma_{12}$) distributions peaking a little more at 90° and 180°, respectively. Since the lowest energy singlet and quintet state are formed from N=3 states with practically identical distributions, the distributions of these N=4 states can be understood to be very much alike as well. By analyzing the individual kinetic and potential energy contributions, we could see that they are very close to those found for the $^4\Sigma_g^-$ state, although the latter attains a slightly more attractive (by 0.1 cm^{-1}) average He-He interaction.

3. Excited solvent states

a. The (^{3}He)$_2$-Cl$_2$ case We found that the excited $\kappa = +1$ states for N=2 are very similar to those obtained for the T-shaped potential case. Thus, the $\Delta\mathcal{E}$ values differ by less than 0.02 cm^{-1}. The first excited singlet and triplet involve a He-He bending excitation mode within the equatorial ring plane, the angular pair density distributions (see top panel of Fig. 5) resembling those obtained for the first-excited particle-in-a-box states in [27] and [28] by using T-shaped He-dopant potentials. The second excited singlet, the $^1\Delta_g$ state, is also a ring-like state (see Fig. 4). As the lowest triplet state, it involves an overall rotation mode around the Z axis. Therefore, the pair density distribution is quite close to that obtained for the ground state. The second excited triplet (the $^3\Sigma_g^+$ state) is the lowest-energy $\kappa = +1$ state that poses helium density at the chlorine ends (see Fig. 4). It can be very well described by a single $(1\sigma_g)(2\sigma_g)$ reference configuration. Consequently, the angular pair density distribution is peaked at $\gamma_{12} = 90^\circ$ and the radial pair density distribution is shifted to a shorter R_{12} value as compared to the ground-state density.

The wavefunction structure for $\kappa = -1$ states is rather simple. They attain a clear dominant $(1r.l)(1\sigma_u)$ configuration, where $1r.l$ refers to a $1\sigma_g$, $1\pi_u$, and $1\delta_g$ ring-like orbitals for Σ, Π, and Δ states, respectively. In fact, the energy splitting between these states match almost perfectly with the energy differences among the corresponding $1r.l$ orbitals. In Table II, we can also see that the states having the same spatial symmetry but different spin multiplicity are almost degenerated. These states obviously differ in having a $1\sigma_u$ orbital with a spin-up or spin-down ^{3}He atom, with the degeneration arising from the negligible exchange contribution with the $1r.l$ orbitals. Similarly, as a consequence of the quasi-degeneration between the $2\sigma_g$ and $1\sigma_u$ orbitals, the total energies of the $^3\Sigma_g^+$ and $^3\Sigma_u^+$ states differ by less than 0.03 cm^{-1}. This high-energy degeneracy persists for larger cluster sizes.

b. The (^{3}He)$_3$-Cl$_2$ case All the states within the $\kappa = +1$ manifold but the $^4\Pi_u$ state are ring-like states, having almost identical one-particle density distributions (see Fig. 4). As for the T-shaped potential case (see Fig. 8 of [20]), the $^4\Delta_g$ state involves an excited He-He vibration mode. The associated angular and radial pair density distributions are two-side-peaked and differ largely from the distributions attained by the rest of ring-like states, which are practically identical. As mentioned above, the first excited quadruplet state is of Π_u symmetry while the Φ_u state, which is more stable by using T-shaped model potentials,

is found to be 0.07 cm^{-1} higher in energy. The pair density distributions associated to the Π_u state (see Fig. 5) suggest that the most probable structure may be T-shaped and planar with two ^{3}He atoms located on the equatorial plane and at opposite sides of a vector of $\sim 2\times R_e^T$ length, with another ^{3}He atom along the molecular axis at a distance $\sim R_e^L$ from the dopant's center of mass (R_e^L indicating the equilibrium distance on the L-well). In this way, the angular pair density is two-side-peaked at γ_{12}=90° and γ_{12}=180°. On the other hand, the radial pair density distributions are broader than for N=2 owing to the overlapping of maxima attained at different R_{12} values. Very similar distributions are attained by the $^4\Pi_g$ and $^2\Pi_g$ ($\kappa = -1$) states, which can be described with a single $(1\sigma_g)(1\pi_u)(1\sigma_u)$ configuration.

The $^2\Sigma_u^+$ state for N=3 is formed from the $^1\Sigma_g^+$ state for N=2 after filling the $1\sigma_u$ orbital with one ^{3}He atom and the τ values associated to *r.l.* orbitals for the $^1\Sigma_g^+$ states are therefore practically conserved. Similarly, the higher energy $^2\Sigma_u^-$ and $^4\Sigma_u^-$ states have the same wavefunction structure that the N=2 $^3\Sigma_g^-$ state but with an additional filled $1\sigma_u$ orbital. Thus, the energy difference among $^{2,4}\Sigma_u^-$ and $^2\Sigma_u^+$ states is practically the same compared to the energy difference between the $^3\Sigma_g^-$ and $^1\Sigma_g^+$ states for N=2. By considering that the $^3\Sigma_g^-$ state poses a $D(\gamma_{12})$ distribution with the maximum region close to $\gamma_{12} = 90°$, it can be understood that the distributions associated to the $^2\Sigma_u^-$ and $^4\Sigma_u^-$ states are all peaked at $\gamma_{12} = 90°$. Summarizing, the wavefunction structures of all the lowest $\kappa = -1$ states for N=3 can be correlated to those obtained for the lowest-energy states for N=2, that are practically unchanged.

c. The (^{3}He)$_4$-Cl_2 case Focusing on the results for $\kappa = +1$ (N=4) states in Table II and Figure 4, we find that only the $^1\Sigma_g^+$ and $^5\Delta_g$ states are ring-like states. Their characteristics are very similar to those found by using T-shaped He-dopant potentials. Both states share very similar pair distributions (see Figs. 5 and 6) that have previously been discussed in [20]. As for N=2 and 3, the $\kappa = -1$ states are formed by adding an extra ^{3}He atom on the $1\sigma_u$ orbital to the lowest-energy $N-1$ ring-like states, with the "source" state obviously depending on the specific symmetry. Accordingly, the $^{1,3}\Sigma_u^-$, $^{1,3}\Pi_g$, $^{1,3}\Delta_u$, and $^5\Phi_g$ states correlate with the $^4\Sigma_g^-$, $^2\Pi_u$, $^2\Delta_g$, and $^4\Phi_u$ states of N=3 sized complexes, with the energy ordering differing by less of 0.01 cm^{-1} to those obtained for the "source" N=3 states. All these N=4 states have very similar one- and two-particle density distributions, as can be inferred from the practically identical distributions of the "source" states. As compared to the angular pair density distributions for N=3, we can observe that a similar weighted peak

to the one located at $\gamma_{12} = 180°$ is formed and that the shoulder at $\gamma_{12} = 70°$ is suppressed. These distributions suggest that T-shaped are the most stable structures with either two ^{3}He atoms at the two ends of the molecule with another two ^{3}He atoms at opposite ends on the ring encircling the dopant or four ^{3}He atoms on the ring plane. The different distributions associated to the $^5\Delta_u$ state can be understood by taking into account that the "source" state (the $^4\Delta_g$ state) also has a different distribution (it involves He-He bending excitation modes). We have also found that the wave-function structures of the $\kappa = +1$ $^3\Delta_g$, $^{3,1}\Pi_u$ and $^3\Phi_u$ states are very similar to those attained by their $\kappa = -1$ counterparts but with the $1\sigma_u$ orbital replaced by the $2\sigma_g$ one. As a result, they display quite similar distributions and the energy difference (0.04 cm^{-1}) is the same as the difference between the $1\sigma_u$ and $2\sigma_g$ orbitals.

Owing to the additional mixing existing between the original $1\sigma_g$ and $2\sigma_g$ orbitals (see Fig. 3), the $^3\Sigma_g^-$ and $^1\Delta_g$ states become more stabilized than their ungerade parity counterparts, with the energy difference (~ 0.1 cm^{-1}) being more than twice the difference between the $1\sigma_u$ and $2\sigma_g$ orbitals.

It is worth noticing that the nature of the solvent states can also be distinguished by the $\langle \mathbf{L}^2 \rangle$ averages listed in Table II. Thus, the expectation values $\langle \mathbf{L}_x^2 + \mathbf{L}_y^2 \rangle$ associated to states posing density at the Cl_2 ends are about 3 or 2 units higher, depending on the mixing between the $1\sigma_g$ and $2\sigma_g$ orbitals. In contrast to the model T-shaped case, the quasi-linear scaling of the $\langle \mathbf{L}^2 \rangle$ averages as a function of N break down for N=4. But in any case, ground-state energies change continuously regardless the form for the He-Cl_2 potential as in [17]. This raises the question of the existence of shell-closure effects (i.e., enhanced stabilities at completion of the annular ring sub-shell). In view of our results, it is not possible to answer this question in general terms. In this way, the mixing between a ring-like and the $2\sigma_g$ orbital for the ground-state seems to point out a smooth transition when filling the second sub-shell for N=4. However, many solvent low-lying ring-stacker-like states are formed from the "sudden" filling of either a $2\sigma_g$ or a $1\sigma_u$ orbital with one ^{3}He atom. Overall, the high degeneration degree attained by ring-like states and the manifold of ring-stacker-like states for N=4, indicates that this cluster size is special among those considered in this work. We should also consider that the non-adiabatic couplings induced by the molecular rotation between these nearly degenerate states could indeed enhance the stabilization of the ground-state as compared to other N-sized clusters. Alternatively, the stabilization of additional quantum excitations at N=4, that obviously affects the equilibrium cluster

population, could be interpreted as a sign of "magicity" in line with the combined experimental/theoretical study by Brühl et al. [39] (i.e., giving rise to a maxima in the ratio between the partition functions for N=3 and 4). Therefore, it cannot be ruled out that N=4 is a "magic number" from the results shown here. Further calculations for $N \geq 5$, including non-adiabatic couplings, would be clarifying if this is indeed the case.

V. VIB-ROTATIONAL DOPANT RAMAN SPECTRA USING A T-SHAPED MODEL AND *AB INITIO* HE-DOPANT POTENTIALS

In Figs. 7(a) and (b), the more intense Q branches for N=1 and 3 are displayed whereas a plot of R and S branches for N=2 and 3 is shown in Fig. 7(c). These figures display continuum profiles of the intensity of the scattered photon in terms of the energy loss between the incident and the exiting photons, $\hbar w_0$ - $\hbar w_{fi}$, measured with respect to the forbidden transition of the bare dopant (J,v)=(0,1) $\leftarrow$ (0,0), 554.37 cm^{-1}. The main lines contributing to the different profiles are specified as T(J,S) where $T = Q, R, S, \cdots$ denote the transition, J=J_i, and S already defines the corresponding values of Λ and $\langle \mathbf{L}^2 \rangle$ involved in Eq. 4. By comparing the spectra for N=1 and N=3, we can appreciate that apart from a blue-shift of 0.012 cm^{-1} for the cluster containing three fermions, the profile displayed in Figure 7 is more congested as there are several contributing lines coming from nearly degenerated spin multiplets, giving rise to peaks of comparable intensity. As a result, the apparent half-width for N=3 is more than double than that for the triatomic. As mentioned in the previous section, the lowest-energy spin multiplets define an overall rotation around the Z axis with an energy difference with respect to the ground state, posing a Λ value equal to zero for all the cases, roughly given by $\frac{\mathrm{B_{eff}}\Lambda^2}{N}$. Therefore, the increased congestion of the spectrum is easily understood. Some of these states (i.e., the $^3\Pi$ state for N=2 or the $^5\Delta_g$ state for N=4) are obviously forbidden by symmetry in doped ^{4}He clusters. Fig. 7(c) depicts the S region of N=2 and 3. Two main S branches, S(J_i=0, S=0,1) and S(J_i=1, S=0), do appear for N=2 whereas the intensity of the R branches is negligible. In contrast, for N=3, in addition to a larger number of S branches, there are comparable R branches coming from its fermionic nature (i.e., the total spin is always a half-integer). For N=4, the top panel of Figure 8 displays the Q main branch. In this particular case, we have added the spin projection, Σ, as a subscript to characterize the states responsible for the main lines. The

Q main branch for N=4 is shifted by about 0.015 cm^{-1} with respect to N=1, its apparent half-width being three times larger. It is worth mentioning that both the blue-shift and the half-width for N=4 doubles the values attained for N=2. Interestingly, although the most intense line is associated to the lowest singlet state [i.e., the one with (J,S_Σ)=(0,0)], the lines coming from the first excited triplet state (the $^3\Pi_u$ state) contribute most to the total intensity of the spectrum profile. This is due to the fact that the $^3\Pi$ state is very close in energy to the ground state, being also a two-fold degenerated state with an $\langle \mathbf{L}^2 \rangle$ value close to the one of the ground state. As in the case of the lowest-energy spin states, this $^3\Pi$ state also resembles an overall rotation around the Z axis with an excitation energy approximately given by $\frac{\mathrm{B_{eff}}\Lambda^2}{4}$.

We have also simulated the ro-vibrational Raman spectrum by using the *ab initio* PES to describe the He-molecule interaction. The spectra for N=1−3 are rather similar to those obtained by using a semi-empirical PES and are therefore not shown here. For N=4, the bottom panel of Figure 8 displays the Q main branch. We can see that in the *ab initio* PES case, apart from showing a more blue-shifted profile (by $\sim$ 0.01 cm^{-1}) and a less symmetric dressing envelope, there are more contributing lines of comparable intensities due to the quasi-degeneration of different states within the same (N,S) manifold, having in turn very similar $\langle \mathbf{L}^2 \rangle$ values (see Table II). Thus, the apparent half-width of the spectral profile in Fig. 8 is about 1.3 times larger than that obtained by using a semi-empirical PES. We should stress however, that both Coriolis and $\mathbf{L}_+\cdot\mathbf{S}_- + \mathbf{L}_-\cdot\mathbf{S}_+$ couplings could break this degeneracy. This analysis is currently in progress. As a consequence of the higher density of stable states when the *ab initio* PES is used, the intensities of the main stick lines are nearly two orders of magnitude larger. For the sake of clarity, the intensities have been renormalized in Fig. 8. In general, the larger intensities come from multiplet states with $\Omega = \Lambda + \Sigma = 0$. In this way, for example, although the $^5\Sigma_u^-$ and $^3\Sigma_g^-$ states are the lowest-energy state for S=2 and 1, the lines that contribute most to the total intensity are associated to the $^5\Delta_g$ and $^3\Pi$ states [i.e., the group of lines with (J,S_Σ)=$(0,2_2)$ and $(1,1_{\pm1})$]. For the same reason, although the $^1\Pi_u$ state is the lowest-energy singlet state, the $^1\Sigma_g^+$ state contributes more to the intensity [i.e., the line with (J,S_Σ)=(0,0)]. However, in the case of other branches such as $R(1)$, - not shown for the sake of clarity - the larger intensities come from states with $\Omega = 1$, in such a way that the $^3\Sigma_g^-$ state is responsible for more than 90% of the intensity. Apart from the selection rules for a specific branch, favoring particular spin and spatial-symmetry

states, we should also consider that although a solvent state is more stable if its rotational $\langle \mathbf{L}^2 \rangle$ contribution is also higher, the total Boltzmann weight can also be lower and thus the intensity of the spectral line. Regardless the used He-dopant PES, the lower the temperature the more decongested the spectrum in such a way that we found that the only line with significant intensity in the Q branch comes from the $^1\Sigma_g^+$ state at temperatures at low as T=0.1 K, as clearly apparent in the inset of Figure 8.

VI. CONCLUDING REMARKS

Our previous study of $(^3\mathrm{He})_N$-$\mathrm{Cl}_2(B)$ clusters has been extended in this paper by means of an enhanced version of the FCI-NO approach [20], considering the dopant species in the ground state and both semi-empirical T-shaped and *ab initio* He-dopant potentials, as well as simulating the Raman dopant spectrum. Provided that the semi-empirical T-shaped PES is used, having a single minimum, the results are very similar to those obtained for $\mathrm{Cl}_2(B)$ [20] and $\mathrm{Br}_2(X)$ [22]. As in [22], this is attributed to the very similar anisotropy of the used He-dopant T-shaped potential functions, with the actual strengths of the associated He-dopant interaction on the global minimum playing a minor role. As in previous cases, the favored clustering of ^{3}He around the host molecule is such that the He-dopant potential interaction is maximized and also takes advantage of the very weak He-He attractive interaction (as found in [40]). In this way, the global He-He interaction per pair is negative and scales linearly with N, with the ^{3}He atoms tending to form pairs around the broad ring encircling the dopant. The excitation spectrum low edge is mainly determined by the independent-particle N=1 Hamiltonian, fermionic statistics, and a highly repulsive on-site interaction that prevents the double occupation of orbital sites, while they tend towards a single occupation as the cluster grows in size. The ro-vibrational Raman simulation of the dopant indicates, in agreement with previous studies [16], that the congestion of the spectrum for fermionic clusters comes from the quasi-degeneration of different spin-multiplets, with the lowest-energy one always corresponding to Λ=0 whereas higher energy states with Λ>0 involves global rotations around the molecular axis with an excitation energy of about $\frac{\mathrm{B_{eff}}\Lambda^2}{N}$. These quantized rotational excitations do not distort the ring-like structures of the clusters, so that the one- and two-particle distributions attained by the lowest-energy spin-multiplets are very similar. Summarizing, the increasingly more congested spectrum in small doped

^{3}He clusters with a highly anisotropic T-shaped He-dopant PES, as the equatorial ring subshell is filling, is attributed to the decreased frequency for the global rotation motion around the molecular axis. As regards to ^{4}He clusters, it is demonstrated that some of these states are missing due to the symmetry condition for the wavefunction.

When the *ab initio* PES is used, the equatorial ring around the Cl_2 axis is formed from N=1 up to 3. For N=4 however, the ground-state He density is already significant at the two ends of Cl_2, with the molecule becoming fully solvated. Nevertheless, solvent ring-like states get very close in energy. An analysis of the microscopic interactions governing the transition to the "full-coated" regime for the ground-state reveals that, departing from the classical picture of a more repulsive He-He interaction as the ring gets more crowded, the increased kinetic energy for the lowest ring-like state at N=4 is not counterbalanced by its higher He-dopant and short-range He-He attraction, causing the flowing of He atoms off the T-shaped well. On the other hand, there are many low-lying (ring-stacker-like) states posing distributions which peaked on both T-shaped and linear configurations as a consequence of the very weak coupling between ^{3}He atoms located in the two L-wells and their small exchange contribution with ^{3}He atoms located on the annular ring. As a consequence of the quasi-degeneration between the ensemble of ring-stacker-like and ring-like states, the congestion of the Raman spectrum for N=4 is even more pronounced than in the T-shaped PES case. Whatever the used He-dopant PES be, a decongested spectrum is recovered when the temperature is lowered at a value (0.1 K) that is still higher than the transition temperature to superfluidity of liquid ^{3}He. Further spectroscopic probes of the dopant at different temperatures, including $\mathbf{L}_- \cdot \mathbf{S}_+ + \mathbf{L}_+ \cdot \mathbf{S}_-$ and Coriolis couplings between the low-lying solvent states [41], could provide a rigorous test of the possible onset of microscopic superfluity in small ^{3}He clusters and its interplay with the appearance of He density at the ends of the host molecule and the decoupling of the He total angular momentum from the molecular rotation, as shown in the case of small ^{4}He clusters in experimental [3] and path integral Monte Carlo simulations [4–6]. Work in this direction is currently in progress.

ACKNOWLEDGMENTS

This work has been partially supported by the CSIC-CAM, CICYT, and MICINN-CSIC Spanish Grants Nos. CCG08-CSIC/ESP-3680, FIS2007-62006 and 2007501004. The Centro de Supercomputación de Galicia (CESGA) and the Centro de Supercomputación y Visu-

alización de Madrid (Ref. AB01101001) are acknowledged for allocation of computer time. We would like to thank M.I. Hernández and A. Hernando for very useful discussions.

---

[1] J. P. Toennies and A. F. Vilesov, Angew. Chem., Int. Ed. **43**, 2622 (2004).

[2] S. Grebenev, J. P. Toennies, and A. F. Vilesov, Science **279**, 2083 (1998).

[3] L. A. Surin, A. V. Potapov, B. S. Dumesh, S. Schlemmer, Y. Xu, P. L. Raston, and W. Jäger, Phys. Rev. Lett. **101**, 233401 (2008).

[4] S. Moroni, A. Sarsa, S. Fantoni, K. E. Schmidt, and S. Baroni, Phys. Rev. Lett. **90**, 143401 (2003).

[5] F. Paesani, K. Kwon, and K. B. Whaley, Phys. Rev. Lett. **94**, 15401 (2005).

[6] Y. Xu, N. Blinov, W. Jäger, and P. N. Roy, J. Chem. Phys. **124**, 081101 (2006).

[7] F. Paesani, A. Viel, F. A. Gianturco, and K. B. Whaley, Phys. Rev. Lett. **90**, 073401 (2003).

[8] S. Moroni, N. Blinov, and P. N. Roy, J. Chem. Phys. **121**, 3577 (2004).

[9] H. Li, N. Blinov, P.-N. Roy, and R. L. Roy, J. Chem. Phys. **130**, 144305 (2009).

[10] P. Jungwirth and A. Krylov, J. Chem. Phys. **115**, 10214 (2001).

[11] M. P. de Lara-Castells, R. Prosmiti, D. López-Durán, G. Delgado-Barrio, P. Villarreal, F. A. Gianturco, and J. Jellinek, Int. J. Quantum Chem. **107**, 2902 (2007).

[12] O. Roncero, R. Pérez-Tudela, M. P. de Lara-Castells, R. Prosmiti, G. Delgado-Barrio, and P. Villarreal, Int. J. Quantum Chem. **107**, 2756 (2007).

[13] O. Roncero, M. P. de Lara-Castells, G. Delgado-Barrio, P. Villarreal, T. Stoecklin, A. Voronin, and J. C. Rayez, J. Chem. Phys. **128**, 164313 (2008).

[14] A. Valdés, R. Prosmiti, P. Villarreal, and G. Delgado-Barrio, J. Chem. Phys. **125**, 014313 (2006).

[15] X. Wang, T. Carrington, Jr., and A. McKellar, J. Phys. Chem. A **113**, 13331 (2009).

[16] D. López-Durán, M. P. de Lara-Castells, G. Delgado-Barrio, P. Villarreal, C. Di Paola, F. A. Gianturco, and J. Jellinek, Phys. Rev. Lett. **93**, 053401 (2004).

[17] M. P. de Lara-Castells, D. López-Durán, G. Delgado-Barrio, P. Villarreal, C. Di Paola, F. A. Gianturco, and J. Jellinek, Phys. Rev. A **71**, 033203 (2005).

[18] M. Barranco, R. Guardiola, S. Hernández, R. Mayol, J. Navarro, and M. Pí, J. Low Temp.

Phys. **142**, 1 (2006).

[19] M. P. de Lara-Castells, G. Delgado-Barrio, P. Villarreal, and A. O. Mitrushchenkov, J. Chem. Phys. **125**, 221101 (2006).

[20] M. P. de Lara-Castells, G. Delgado-Barrio, P. Villarreal, and A. O. Mitrushchenkov, J. Chem. Phys. **131**, 174110 (2009).

[21] M. P. de Lara-Castells, A. O. Mitrushchenkov, G. Delgado-Barrio, and P. Villarreal, Few-Body Syst. **45**, 233 (2009).

[22] M. P. de Lara-Castells, G. Delgado-Barrio, P. Villarreal, and A. O. Mitrushchenkov, Int. J. Quantum Chem. (2010), Microscopic description of small doped ^{3}He clusters through the Full-Configuration-Interaction Nuclear Orbital approach: the $(^3\mathrm{He})_N$-$\mathrm{Br}_2(X)$ case revisited, in press.

[23] S. S. Huang, C. R. Bieler, K. C. Janda, F. Tao, W. Klemperer, P. Casavecchia, G. Volpi, and N. Halberstadt, J. Chem. Phys. **102**, 8846 (1995).

[24] W. D. Sands, C. R. Bieler, and K. C. Janda, J. Chem. Phys. **95**, 729 (1991).

[25] Z. Bačić, M. Kennedy-Mandziuk, J. M. Moskowitz, and K. E. Schmidt, J. Chem. Phys. **97**, 6472 (1992).

[26] M. A. MacMahon and K. B. Whaley, J. Chem. Phys. **103**, 2561 (1995).

[27] P. Villarreal, O. Roncero, and G. Delgado-Barrio, J. Chem. Phys. **101**, 2217 (1994).

[28] M. I. Hernández, N. Halberstadt, W. D. Sands, and K. C. Janda, J. Chem. Phys. **113**, 7252 (2000).

[29] T. Takayanagi, M. Shiga, and T. Taketsugu, Theor. Comp. Chem. **109**, 43 (2005).

[30] A. García-Vela, J. Chem. Phys. **122**, 014312 (2005).

[31] K. P. Huber and G. Herzberg, *Constants of Diatomic Molecules*, Van Nostrand Reinhold, New York, 1979.

[32] V. Aquilanti, D. Cappelletti, V. Lorent, E. Luzzatti, and F. Pirani, J. Phys. Chem. **97**, 2063 (1993).

[33] L. Beneventi, P. Casavecchia, G. G. Volpi, C. R. Bieler, and K. C. Janda, J. Chem. Phys. **98**, 178 (1993).

[34] S. M. Cybulski and S. J. Holt, J. Chem. Phys. **110**, 7745 (1999).

[35] J. C. Wheatley, Rev. Mod. Phys. **47**, 415 (1975).

[36] G. Maroulis, Mol. Phys. **77**, 1085 (1992).

[37] P. M. Felker, J. Chem. Phys. **125**, 184313 (2006).

[38] J. Hubbard, Proc. R. Soc. London Ser. A **276**, 238 (1963).

[39] R. Brühl, R. Guardiola, A. Kalinin, O. Kornilov, J. Navarro, T. Savas, and J. P. Toennies, Phys. Rev. Lett. **92**, 185301 (2004).

[40] P. Barletta, A. Fabrocini, A. Kievsky, J. Navarro, and A. Polls, Phys. Rev. A **68**, 053205 (2003).

[41] M. P. de Lara-Castells, A. Mitrushenkov, P. Palmieri, F. L. Quére, C. Leonard, and P. Rosmus, Mol. Phys. **98**, 1713 (2000).

	$(N,\, S)$							
a)	(1,1/2)	(2,0)	(2,1)	(3,1/2)	(3,3/2)	(4,0)	(4,1)	(4,2)
	$-14.09(\sigma_g)$	$-28.06(\Sigma_g^+)$	$-27.83(\Pi_u)$	$-41.58(\Pi_u)$	$-41.73(\Sigma_g^-)$	$-54.52(\Sigma_g^+)$	$-54.53(\Sigma_g^-)$	$-54.04(\Delta_g)$
$\Delta\mathcal{E}$	$0.46(\pi_u)$	$0.82(\Pi_u)$	$0.31(\Sigma_g^-)$	$0.43(\Delta_g)$	$1.25(\Phi_u)$	$0.44(\Delta_g)$	$0.13(\Pi_u)$	$2.55(\Pi_u)$
b)	τ (NO occupation numbers)							
$1\sigma_g$	1.0	1.53	0.99	1.24	0.98	0.94	1.13	0.94
$1\pi_u$		0.40	0.99	1.43	1.89	1.94	1.73	1.82
$1\delta_g$		0.06	0.01	0.27	0.04	0.80	0.79	0.96
$1\phi_u$			0.01	0.04	0.05	0.18	0.24	0.14
$1\gamma_g$				0.01	0.03	0.09	0.06	0.09
$1\eta_u$					0.01	0.02	0.02	0.03
c)	$\langle \mathbf{L}^2 \rangle$							
	3.75	7.45	8.43	12.17	11.13	14.84	14.90	18.98
	4.69	8.52	7.39	15.29	20.48	18.84	15.86	15.95

TABLE I: *a*) FCI energies (in cm^{-1}) of the lowest-energy states of $(^3\mathrm{He})_N$-$\mathrm{Cl}_2(X)$ clusters for each (N, S) manifold using a T-shaped He-dopant model PES. The corresponding $\mathrm{D}_{\infty h}$ symmetry is indicated in parenthesis. Energy differences between the lowest and the first excited state $\Delta\mathcal{E}$ (in cm^{-1}) for each (N, S) manifold are also indicated. *b*) NO occupation numbers, τ, of relevant natural orbitals ($\tau > 0.005$) associated to the lowest-energy states for each (N, S). *c*) Average values $\langle L^2 \rangle$ (a.u.).

N	S	$\kappa = +1$			$\kappa = -1$			$\Delta\mathcal{E}(\mathrm{cm}^{-1})$
		A_g	B_{3u}/B_{2u}	B_{1g}	B_{1u}	B_{2g}/B_{3g}	A_u	
1	1/2	$-\mathbf{10.36}(1\sigma_g)$	-9.81 $(1\pi_u)$	-8.83 $(1\delta_g)$	$-\underline{8.51}$ $(1\sigma_u)$	-4.92 $(1\pi_g)$	-3.08 $(1\delta_u)$	0.55
		$-\underline{8.55}$ $(2\sigma_g)$						
2	0	$-\mathbf{20.53}(^1\Sigma_g^+)$	-19.69 $(^1\Pi_u)$	-19.58 $(^1\Delta_g)$	$-\underline{19.10}$ $(^1\Sigma_u^+)$	$-\underline{18.54}$ $(^1\Pi_g)$	$-\underline{17.58}$ $(^1\Delta_u)$	0.84
	1	$-\underline{19.13}$ $(^3\Sigma_g^+)$	$-\mathbf{20.24}(^3\Pi_u)$	-19.77 $(^3\Sigma_g^-)$	$-\underline{19.10}$ $(^3\Sigma_u^+)$	$-\underline{18.54}$ $(^3\Pi_g)$	$-\underline{17.56}$ $(^3\Delta_u)$	0.29
3	1/2	-29.77 $(^2\Delta_g)$	$-\mathbf{30.19}(^2\Pi_u)$	-29.77 $(^2\Delta_g)$	$-\underline{29.49}$ $(^2\Sigma_u^+)$	$-\underline{29.20}$ $(^2\Pi_g)$	$-\underline{28.72}$ $(^2\Sigma_u^-)$	0.42
	3/2	-28.41 $(^4\Delta_g)$	$-\underline{29.23}(^4\Pi_u)$	$-\mathbf{30.26}(^4\Sigma_g^-)$	$-\underline{28.22}(^4\Delta_u)$	$-\underline{29.20}$ $(^4\Pi_g)$	$-\underline{28.72}$ $(^4\Sigma_u^-)$	1.03
4	0	-39.26 $(^1\Sigma_g^+)$	$-\underline{\mathbf{39.39}}(^1\Pi_u)$	$-\underline{39.07}$ $(^1\Delta_g)$	$-\underline{38.94}$ $(^1\Delta_u)$	$-\underline{39.35}$ $(^1\Pi_g)$	$-\underline{38.94}$ $(^1\Delta_u)$	0.04
	1	$-\underline{38.97}$ $(^3\Delta_g)$	$-\underline{39.39}$ $(^3\Pi_u)$	$-\underline{\mathbf{39.52}}(^3\Sigma_g^-)$	$-\underline{38.94}$ $(^3\Delta_u)$	$-\underline{39.35}$ $(^3\Pi_g)$	$-\underline{39.43}$ $(^3\Sigma_u^-)$	0.09
	2	-38.80 $(^5\Delta_g)$	$-\underline{38.35}$ $(^5\Phi_u)$	-38.80 $(^5\Delta_g)$	$-\underline{37.57}$ $(^5\Delta_u)$	$-\underline{38.32}$ $(^5\Phi_g)$	$-\underline{\mathbf{39.43}}(^5\Sigma_u^-)$	0.63
$\langle \mathbf{L}^2 \rangle$								
4	0	18.70 $(^1\Sigma_g^+)$	23.78 $(^1\Pi_u)$	24.68 $(^1\Delta_g)$	26.30 $(^1\Delta_u)$	23.31 $(^1\Pi_g)$	26.30 $(^1\Delta_u)$	
	1	26.94 $(^3\Delta_g)$	23.68 $(^3\Pi_u)$	20.89 $(^3\Sigma_g^-)$	26.26 $(^3\Delta_u)$	23.16 $(^3\Pi_g)$	22.21 $(^3\Sigma_u^-)$	
	2	22.85 $(^5\Delta_g)$	32.23 $(^5\Phi_u)$	22.85 $(^5\Delta_g)$	25.93 $(^5\Delta_u)$	31.50 $(^5\Phi_g)$	21.92 $(^5\Sigma_u^-)$	

TABLE II: FCI energies (in cm^{-1}) of $(^3\mathrm{He})_N$-$\mathrm{Cl}_2(X)$ clusters using the *ab initio*-based PES from [23]. The states are classified according to the number of fermions (N), the total spin (S) and the symmetry within the D_{2h} point group (the corresponding $D_{\infty h}$ symmetry is indicated in parenthesis). Values in boldface correspond to the lowest energy states within a given (N, S) manifold whereas underlined values are associated to states posing He density at the two ends of Cl_2. For N=4, average values $\langle \mathbf{L}^2 \rangle$ (a.u.) are given.

(ℓ_z)	$\epsilon(\mathrm{cm}^{-1})$	$(N,\, S)$						
		(2,0)	(2,1)	(3,1/2)	(3,3/2)	(4,0)	(4,1)	(4,2)
		$(^1\Sigma_g^+)$	$(^3\Pi_u)$	$(^2\Pi_u)$	$(^4\Sigma_g^-)$	$(^1\Pi_u)$	$(^3\Sigma_g^-)$	$(^5\Sigma_g^-)$
		τ (NO occupation numbers)						
$1\sigma_g(0)$	-10.36	1.55	0.99	1.28	0.98	1.27	1.26	0.98
$1\pi_u(\pm1)$	-9.81	0.36	0.99	1.37	1.89	1.38	1.86	1.88
$1\delta_g(\pm2)$	-8.82	0.08	0.01	0.29	0.05	0.30	0.18	0.05
$1\phi_u(\pm3)$	-6.74	0.01	0.01	0.04	0.05	0.04	0.09	0.05
$1\gamma_g(\pm4)$	-4.91			0.01	0.02	0.01	0.03	0.02
$1\eta_u(\pm5)$	-4.43				0.01		0.01	0.01
$2\sigma_g(0)$	-8.55					0.99	0.55	
$1\sigma_u(0)$	-8.51							0.99

TABLE III: NO occupation numbers, τ, of significant natural orbitals ($\tau > 0.005$) for each (N, S) lowest-energy state of $(^3\mathrm{He})_N$-$\mathrm{Cl}_2(X)$ clusters, using the *ab initio*-based He-$\mathrm{Cl}_2(X)$ PES from [23]. First column indicates $\mathrm{D}_{\infty h}$ symmetries of the NOs (ℓ_z is the orbital angular momentum projection on the Z axis) whereas orbital energies, ϵ, are tabulated in the second column.

	(N)							
	(1)		(2)		(3)		(4)	
	$(1\sigma_g)$	$(2\sigma_g)$	$(^1\Sigma_g^+)$	$(^3\Sigma_g^+)$	$(^4\Sigma_g^-)$	$(^4\Pi_u)$	$(^3\Sigma_g^-)$	$(^1\Sigma_g^+)$
E_{tot} (cm^{-1})	**−10.36**	−8.55	**−20.53**	−19.13	**−30.26**	−29.23	**−39.52**	−39.26
$\langle K \rangle$	8.20	8.77	16.52	17.03	25.19	25.49	33.99	35.08
$\langle V^{He-Cl_2} \rangle$	−18.55	−17.32	−36.82	−35.91	−54.59	−53.98	−71.77	−72.18
$\langle V^{He-He} \rangle$			−0.23	−0.27	−0.86	−0.75	−1.73	−2.16

TABLE IV: Total, kinetic and potential energy contributions associated to the lowest-energy and selected exited states of $(^3He)_N$-$Cl_2(X)$ clusters using the *ab initio*-based He-dopant PES from [23]. Total energy values in boldface correspond to the ground solvent states whereas underlined values are associated to the lowest energy states posing He density at the two ends of Cl_2.

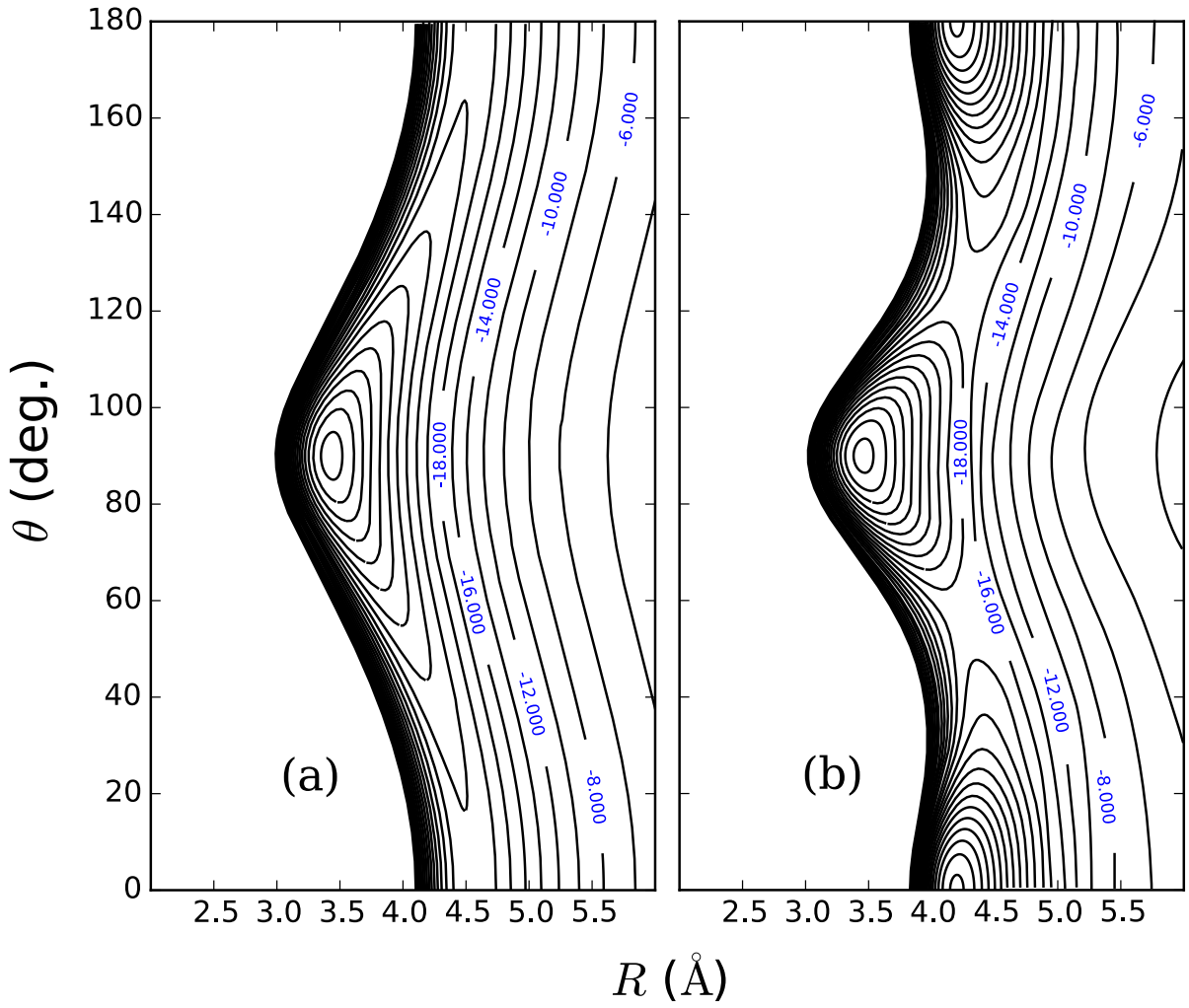

FIG. 1: (color online) Countour plots of the He−$Cl_2(X)$ potential energy surface as a function of distance of the He atom from the Cl_2 center of mass (R) and θ, the angle that **R** forms with the bond direction. Potential values are in cm^{-1}. (a) Left panel for the T-shaped model PES. (b) Rigth panel for the *ab initio*-based PES from [23].

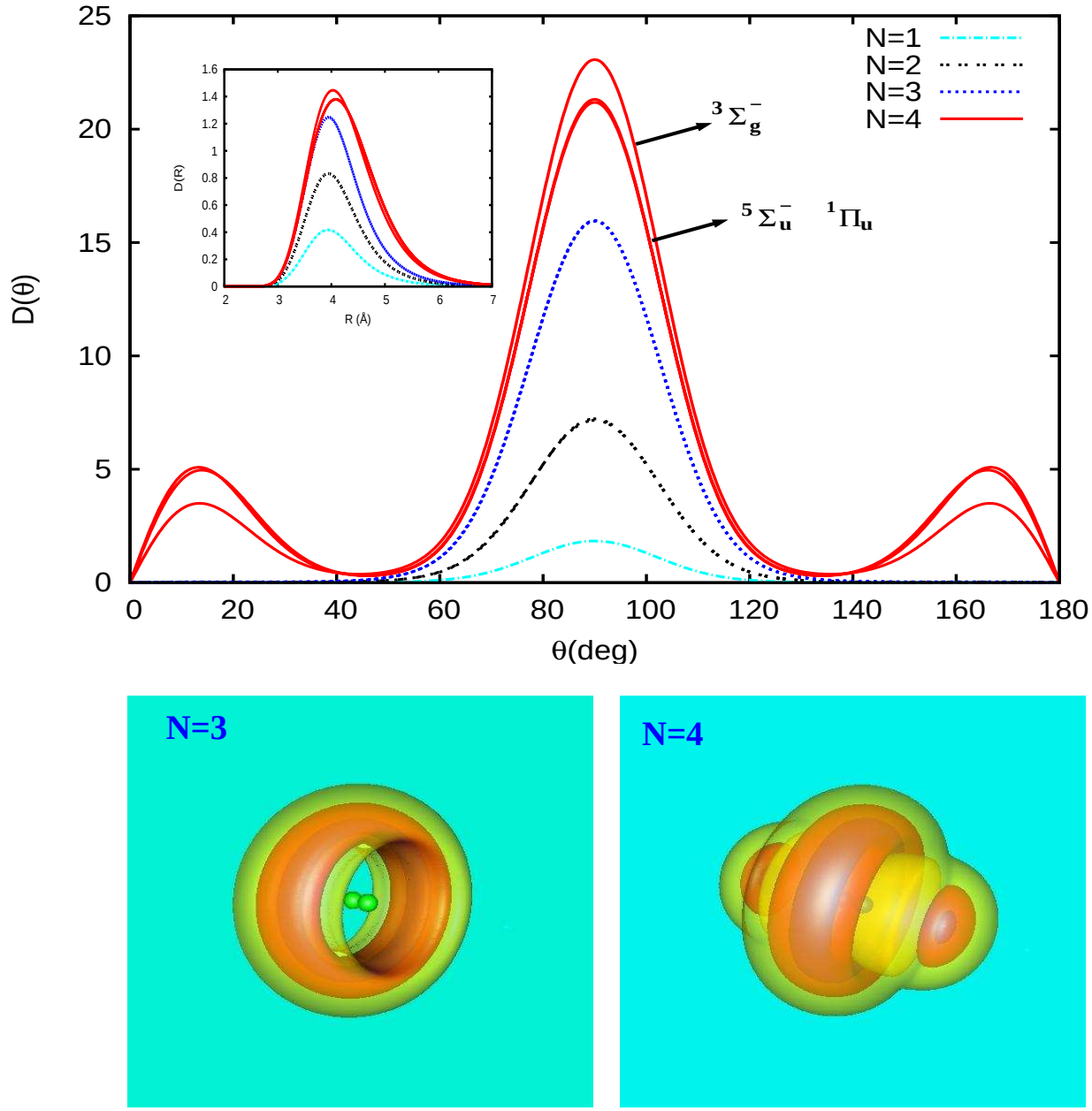

FIG. 2: (color online) Angular Helium density distributions for the lowest-energy states of $Cl_2(X)$-$(^3He)_N$ clusters for each (N,S) manifold (from N=1 up to N=4) using an *ab initio* PES to model the He-Cl_2 interaction. The densities are normalized as $\int D(\theta)d\theta = N$. Inset: Radial density distributions normalized to the number of helium atoms. Bottom panel: Equiprobability density surfaces between $0.001 \times max\{|\rho^{gs}|^2\}$ and $0.5 \times max\{|\rho^{gs}|^2\}$; Left panel for $(^3He)_3$-Cl_2. Right panel for $(^3He)_4$-Cl_2.

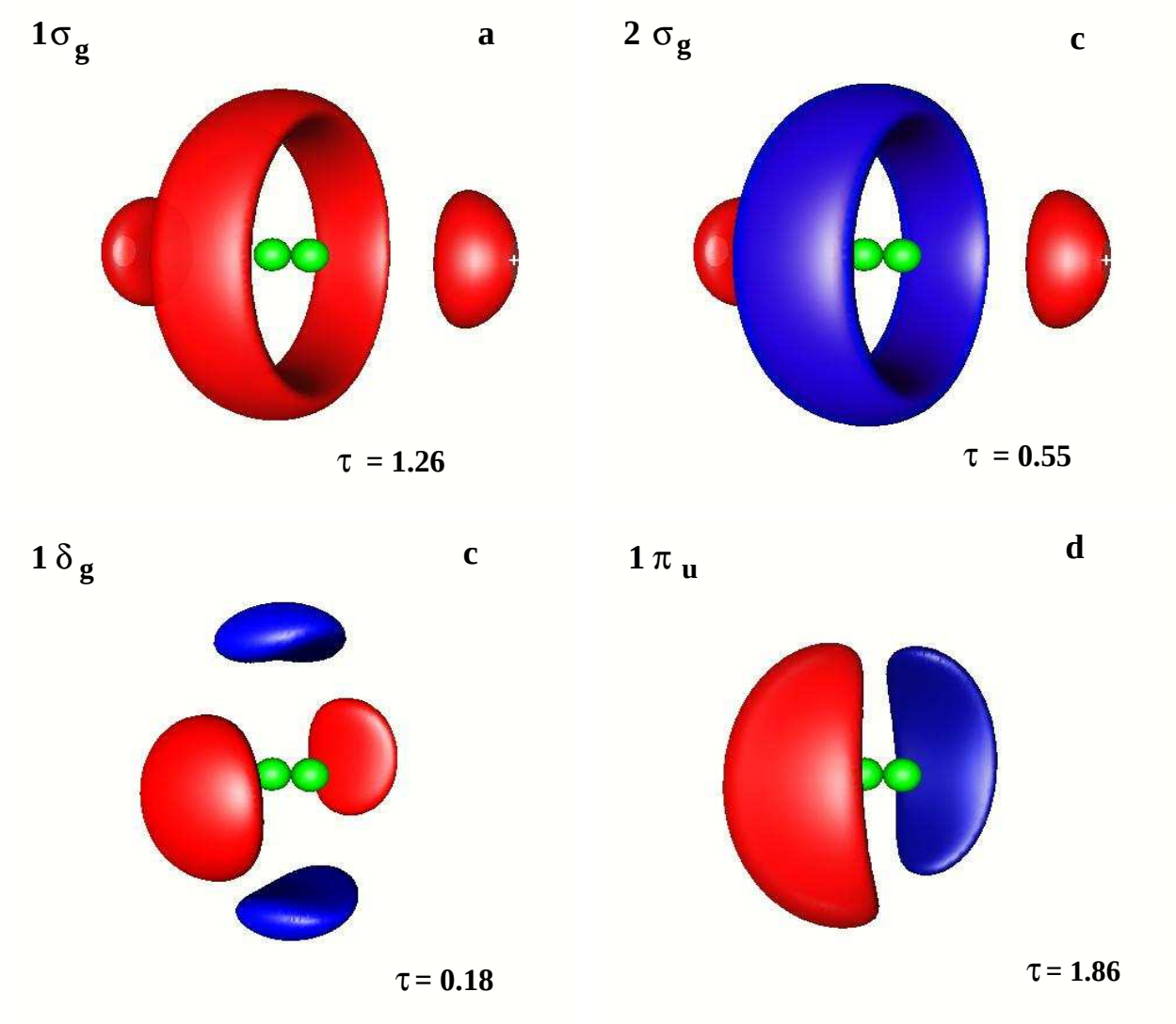

FIG. 3: (color online) Representation of relevant NO iso-probability surfaces for the ground state $(^3\mathrm{He})_4$-$\mathrm{Cl}_2(B)$ complex ($^3\Sigma_u^-$ state) using the *ab initio* model PES from [23]. NO occupation numbers τ are also shown. The positions of the Cl atoms are indicated by green balls. Red and blue colors indicate positive and negative lobes of the orbitals, respectively. The probability values have been selected to be half the maximum value attained at each NO.

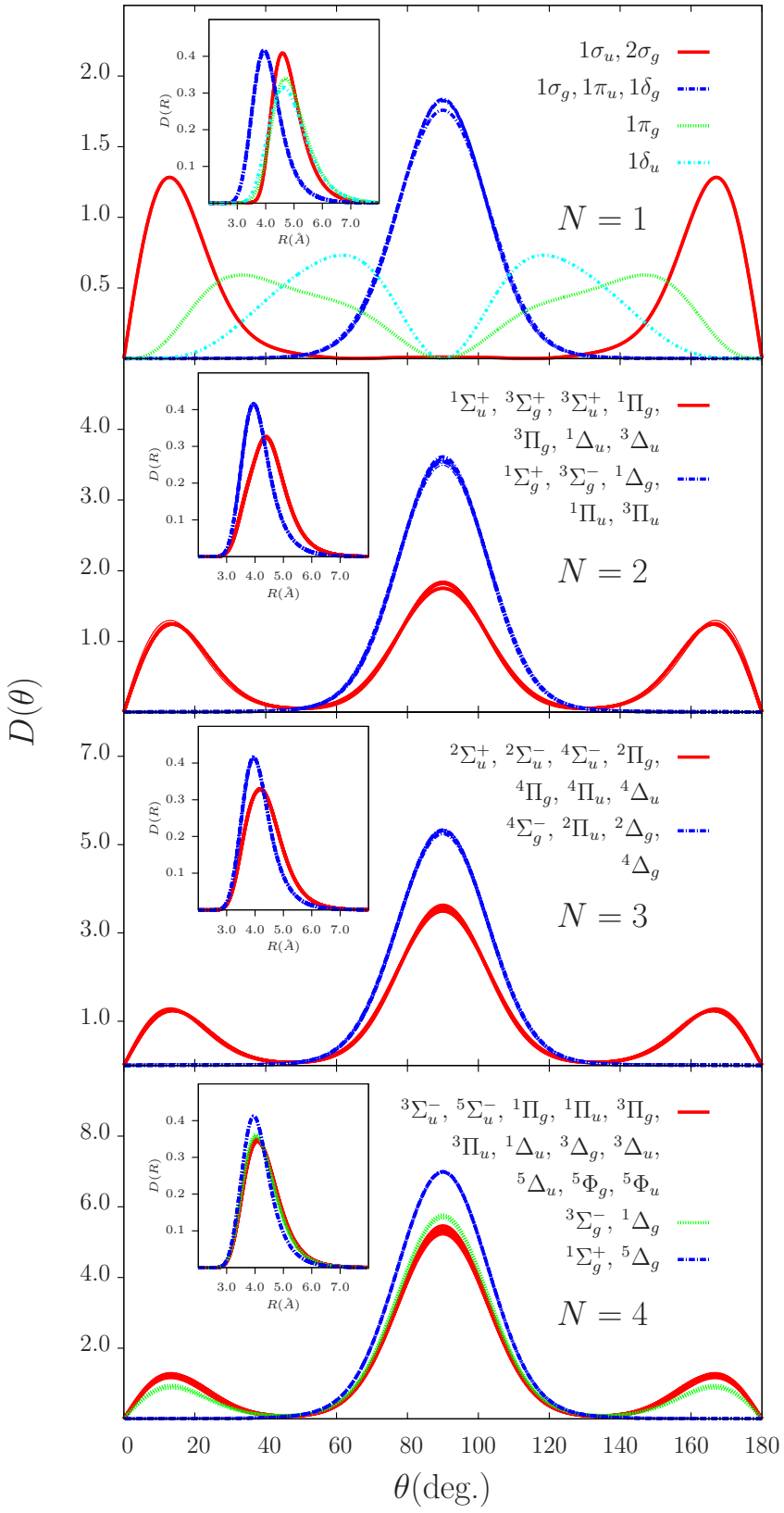

FIG. 4: (color online) Angular He density distributions in the ground and excited states of $(^3\mathrm{He})_N$-$\mathrm{Cl}_2(X)$ clusters using the *ab initio* model PES from [23]. The densities are normalized as $\int D(\theta)d\theta = N$. Inset: Radial density distributions normalized to unity.

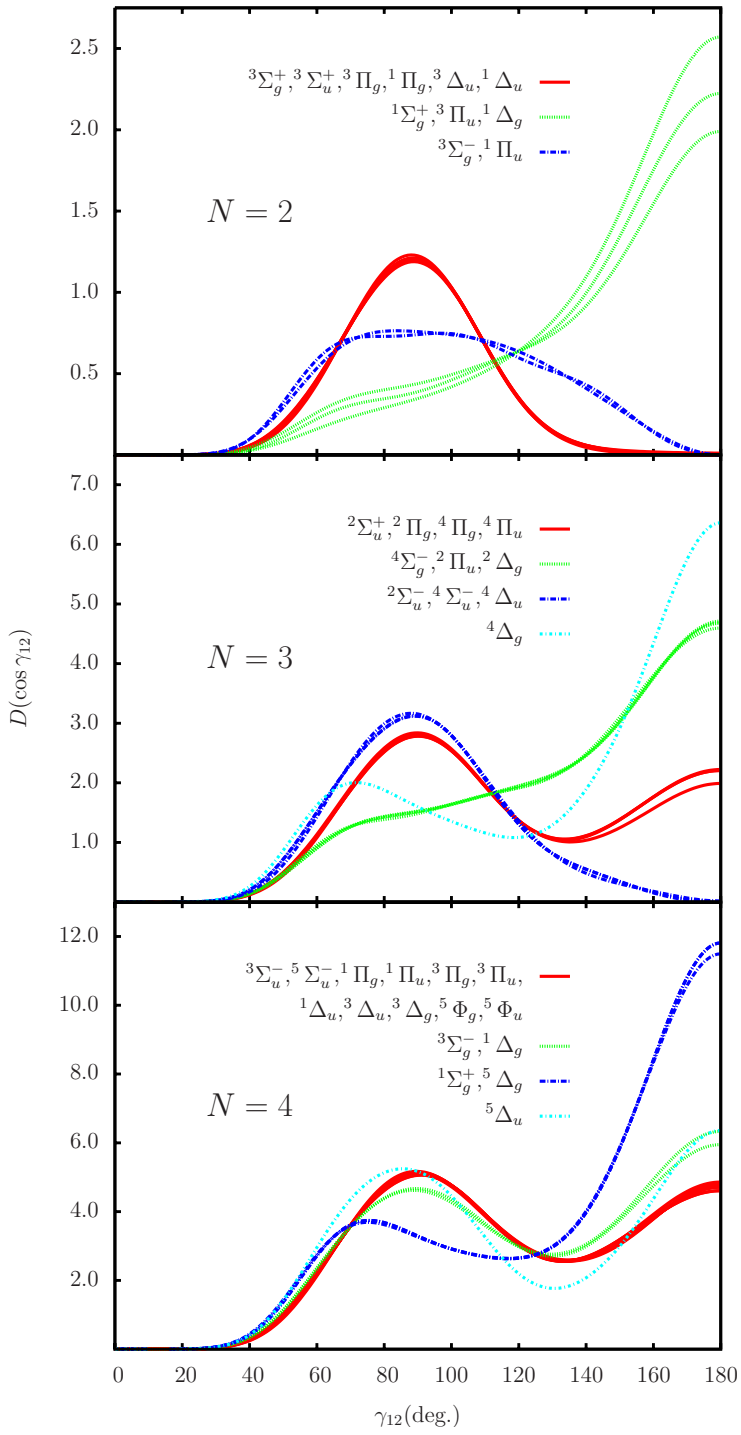

FIG. 5: (color online) Angular two-body density distributions, $D(\cos\gamma_{12})$, in the ground and low-lying excited states of $(^3\mathrm{He})_N$-$\mathrm{Cl}_2(X)$ clusters using the *ab initio* model PES from [23]. The densities are normalized as $\int d\cos\gamma_{12} D(\cos\gamma_{12}) = \begin{pmatrix} N \\ 2 \end{pmatrix}$.

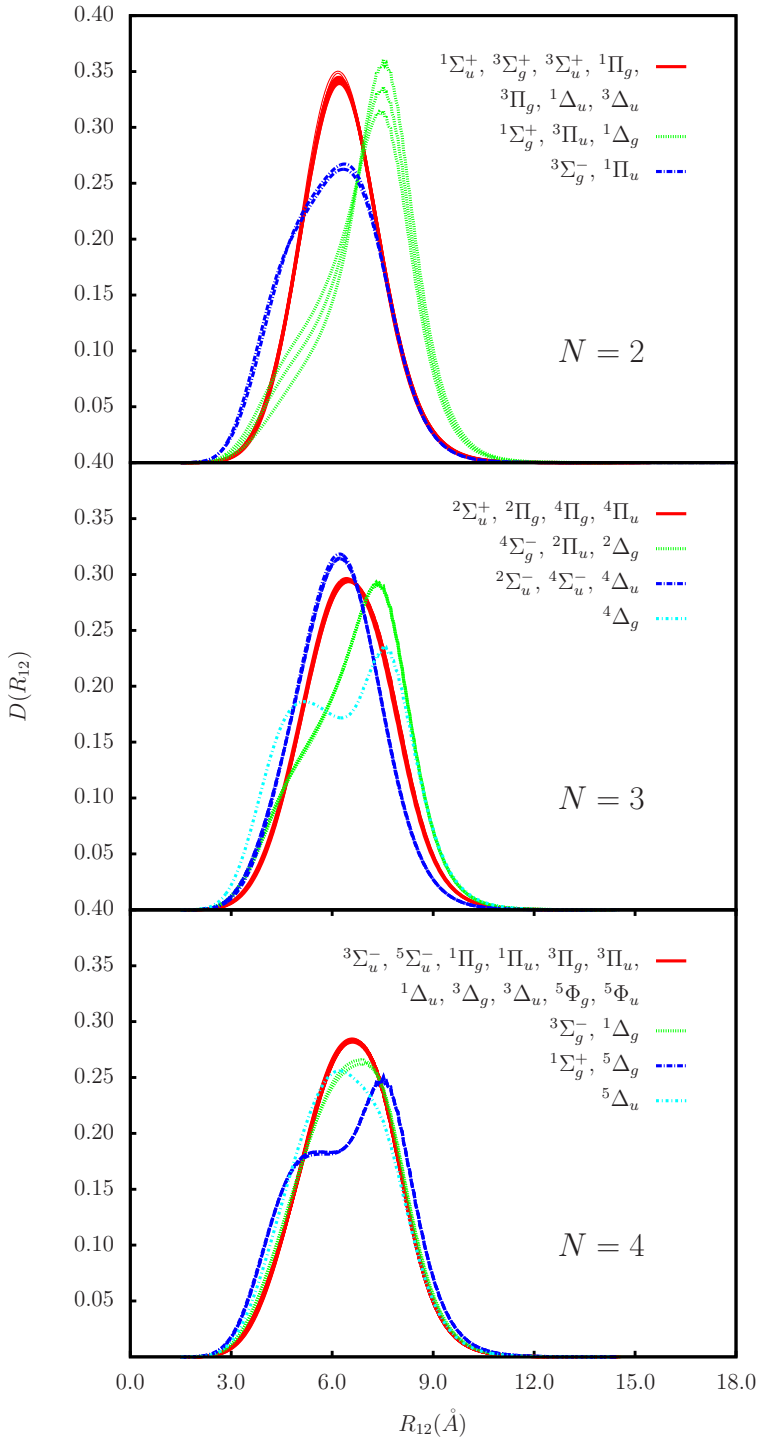

FIG. 6: (color online) Two-body density distributions as a function of the He-He distance, D(R_{12}), in the in the ground and low-lying excited states of $(^3\mathrm{He})_N$-$\mathrm{Cl}_2(X)$ clusters using the *ab initio* model PES from [23]. The densities are normalized as $\int dR_{12} D(R_{12})$=1.

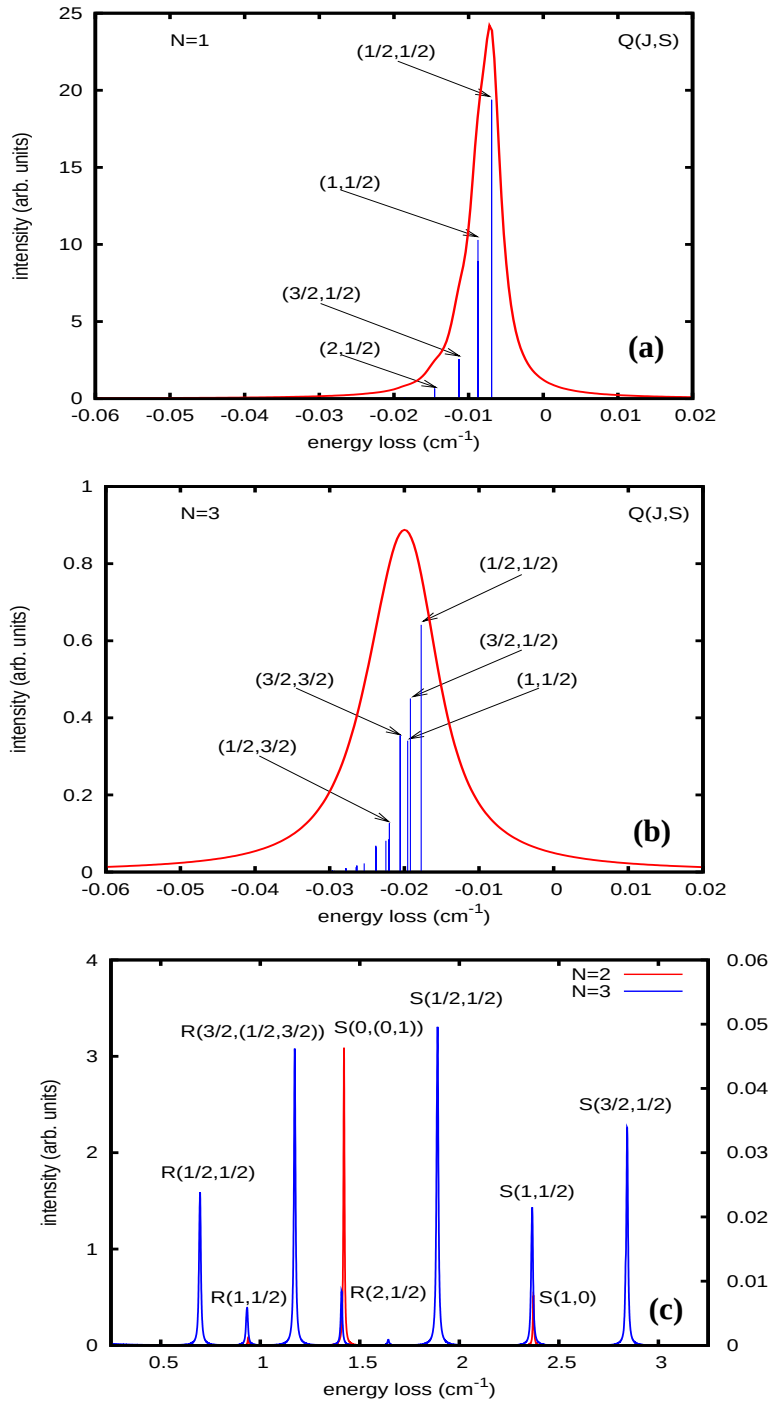

FIG. 7: (color online) Raman simulation spectra in the region of the Q, R and S branches for $Cl_2(X)$ doped helium clusters (T=0.5 K) using a semi-empirical model PES. (a) Q branch for N=1. (b) Q branch for N=3. (c) Main R and S branches for N=2 (left y axis) and N=3 (right y axis).

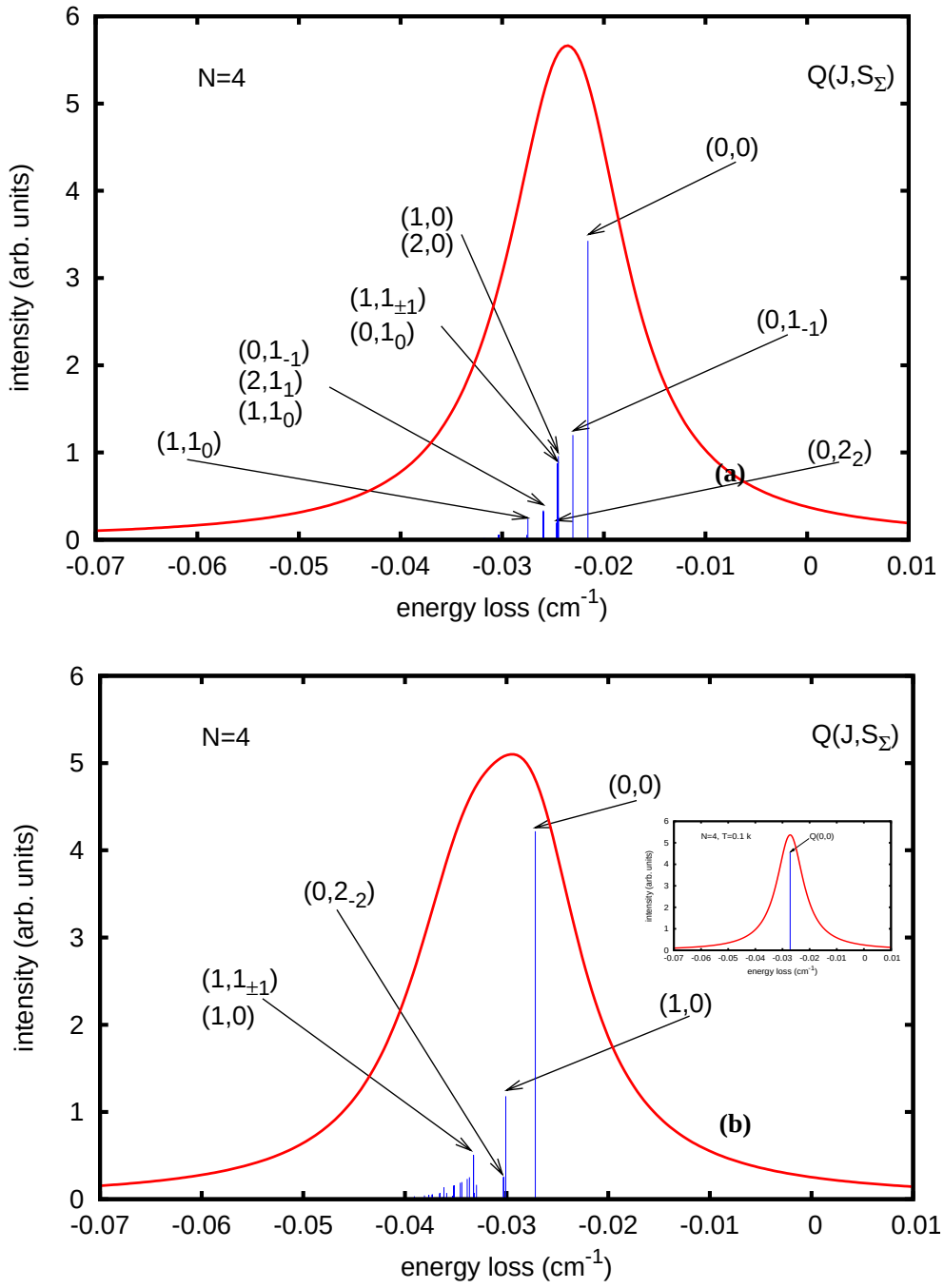

FIG. 8: (color online) Main Q branch of the ($v = 1 \leftarrow 0$) ro-vibrational Raman spectrum of (^{3}He)$_4$-Cl$_2$(X) clusters (T=0.5 K) using (a) a semi-empirical model He-molecule PES (top panel); (b) a fitted PES from *ab initio* calculations (bottom panel). Inset: the same but at a temperature of 0.1 K.